



Studienarbeit

# 3D CAA Investigation of a Circulation Control Airfoil with Coanda flap

Sabrina Haubold B.Sc.  
Matrikelnummer 4453725

Ausgegeben: Prof. Dr.-Ing. J. W. Delfs  
Institut für Aerodynamik und Strömungstechnik  
Abteilung Technische Akustik  
Deutsches Zentrum für Luft- und Raumfahrt

Betreuer: Lennart Rossian

Eingereicht am: 16.03.2020

# Eidesstattliche Erklärung

Hiermit erkläre ich, Sabrina Haubold, geb. am 07.04.1995, des Eides statt, die vorliegende Studienarbeit selbstständig und ohne fremde Hilfe verfasst und keine anderen als die angegebenen Hilfsmittel verwendet zu haben.

Sabrina Haubold,

Braunschweig, 16.03.2020

# Kurzfassung

Lärmemissionen sind ein wichtiger Aspekt im Design von Flugzeugen. Bisher lag der Fokus hierbei auf den Antriebssystemen, welche zuvor den größten Beitrag zum Gesamtlärm der Fluggeräts leisteten. Da nun aber die Lärmemission der Triebwerke mithilfe von lärmreduktionsorientiertem Design, akustischen Absorbern und schallabschattender Platzierung der Triebwerke gesenkt werden konnten, rücken andere Lärmquellen in den Vordergrund.

Der sogenannte Zellenlärm wird sowohl vom Fahrwerk als auch von dem Hochauftriebssystem dominiert. Diese Bauteile produzieren nicht nur viel Schall, sondern kommen außerdem in Bodennähe zum Einsatz, sodass weniger Möglichkeit besteht, dass die Amplitude abklingt oder atmosphärisch gedämpft wird. Diese Studie befasst sich speziell mit dem Hochauftriebssystem.

Ein aktives Hochauftriebssystem in Form einer Coanda Klappe, kombiniert mit einer Senknase an der Vorderkante des Flügelprofils, hat das Potential, einen höheren Auftrieb zu erzeugen als die klassische drei-Element-Konfiguration aus Vorflügel, Flügel und Klappe, wobei es jedoch deutlich weniger Schall produziert. Diese Tatsache konnte 2010 von Pott-Pollenske und Pfingsten in einer Windkanalanalyse nachgewiesen werden. Dennoch könnte ein besseres Verständnis der involvierten aeroakustischen Schallquellen Optionen aufzeigen, wie der Lärm noch weiter reduziert werden kann.

In vorangegangenen zweidimensionalen Simulationen wurden zwei Quellen identifiziert, welche den größten Beitrag zu dem von dieser Konfiguration produzierten Lärm leisten: Krümmungslärm und Hinterkantenlärm an der Klappe. Um zu bestimmen, welche dieser Quellen die dominantere ist, ist es nötig, dreidimensionale Simulationen durchzuführen, welche die dreidimensionale Turbulenz, die für beide dieser Schallquellen essentiell ist, besser berücksichtigen können.

Die Ergebnisse dieser Analyse bestätigen die Funde aus vorangegangenen zweidimensionalen Simulationen. Die Verteilung der akustischen Energie auf verschiedene Frequenzen wird von der 2D Simulation qualitativ erfasst. Die Schalldruckpegel aus der 2D Simulation können korrigiert werden, um eine gute Näherung der aus dreidimensionaler Turbulenz resultierenden Schallspektren zu erreichen. Die Simulationen zeigen eine Dominanz des Hinterkantenlärms in der Abstrahlrichtung nach vorne abwärts, wo Abschattungseffekte den Krümmungslärm reduzieren, während der Krümmungslärm den nach hinten abwärts abgestrahlten Lärm dominiert. Dies führt zu dem Schluss, dass eine Reduktion beider Quellen notwendig wäre, um den am Boden aufgezeichneten Lärm dieser Hochauftriebskonfiguration zu minimieren.



# Abstract

Noise emission is an important aspect of airplane design. The focus so far has been on propulsion systems as the major contributor to aircraft noise. However, as the noise emitted by the engines is reduced through low noise oriented design, acoustic absorbers and strategic placement of the engines to benefit from acoustic shielding, other noise sources shift into focus.

Airframe noise is dominated by both the landing gear and the high lift system. In addition to their significant noise production, both these devices are employed in close proximity to the ground, where there is less opportunity for atmospheric dampening or amplitude decay. The focus of this study is on the high lift system.

An active high lift system such as a Coanda flap, combined with a droop nose at the leading edge, has the potential to achieve higher lift coefficients as the classic three-element-wing configuration while emitting significantly less noise. This was shown in 2010 by Pott-Pollenske and Pflingsten in through wind-tunnel analysis. However, a clearer understanding of the aeroacoustic sources involved could reveal options to reduce noise even further.

In previous two-dimensional simulations, two sources were identified as the most significant contributors to the noise produced by this configuration: curvature noise and trailing edge noise on the flap. To determine, which of these two sources is the dominant one, it is necessary to conduct three-dimensional simulations, in order to accurately capture the three-dimensional turbulence, that is essential for both these sources.

The results of this analysis support the findings of previous two-dimensional simulations. The distribution of acoustic energy across frequencies is captured qualitatively by the 2D simulations. The higher sound pressure levels in the 2D simulation can be corrected for, in order to arrive at a good approximation of the sound spectra produced by three-dimensional turbulence. Simulations show trailing edge noise to be dominant in the radiation towards the lower front, where curvature noise is reduced through shielding effects, while curvature noise dominates the sound radiated aft-downwards. This would suggest, that both sources would need to be reduced in order to minimize the noise footprint of this high lift configuration.



# Contents

<b>Nomenclature</b>	<b>IX</b>
<b>1 Introduction</b>	<b>1</b>
<b>2 Theory</b>	<b>4</b>
2.1 High Lift Configurations . . . . .	4
2.1.1 The Coanda Flap . . . . .	5
2.2 Aeroacoustic Sources . . . . .	5
2.2.1 Trailing Edge Noise . . . . .	7
2.2.2 Curvature Noise . . . . .	8
2.3 Acoustic far-field vs. near-field . . . . .	8
<b>3 Numerical Method</b>	<b>10</b>
3.1 Computational Aeroacoustics . . . . .	10
3.2 PIANO . . . . .	11
3.3 fRPM . . . . .	12
<b>4 Numerical Setup</b>	<b>14</b>
<b>5 Results</b>	<b>17</b>
5.1 Preliminary Simulations . . . . .	17
5.1.1 fRPM Meshes . . . . .	18
5.1.2 PIANO Grid . . . . .	20
5.1.3 Boundary Conditions . . . . .	21
5.1.4 Simulation results of final 2D mesh . . . . .	22
5.2 3D Extrusion . . . . .	22
5.3 Effect of Spanwise Extension on Sound Pressure Levels . . . . .	24
5.3.1 Trailing Edge Source . . . . .	24
5.3.2 Curvature Source . . . . .	29
5.3.3 2D Correction . . . . .	34
5.3.4 Comparison of Both Sources . . . . .	35
<b>6 Conclusion</b>	<b>40</b>
<b>Bibliography</b>	<b>41</b>
<b>List of Figures</b>	<b>44</b>
<b>List of Tables</b>	<b>46</b>
<b>A Appendix</b>	<b>47</b>





# Nomenclature

## Latin Symbols

$a_\infty$	speed of sound
$b$	span of the wing
$c$	chord length of wing profile
$c_y$	scaling constant
$C$	constant for 2D to 3D correction
$C_\mu$	(blowing) momentum coefficient
$C_L$	lift coefficient
$D$	jet diameter
$d_B(x)$	distance of position $x$ from the obstacle/body
$d_S(x)$	distance of position $x$ from the source
$f$	frequency
$h$	blowing slot height
$He$	Helmholtz number
$He_B$	Helmholtz number of an obstacle/body
$He_S$	Helmholtz number of the source
$I_{3D}$	sound intensity
$k$	turbulence kinetic energy
$L$	characteristic length parameter
$l$	spanwise extension of the 3D grid
$l_B$	dimension of obstacle/body
$l_S$	source dimension
$l_{min}$	turbulent length scale of smallest eddies resolved by FRPM
$\dot{m}$	massflow
$M$	Mach number
$M_0$	local mean flow Mach number
$M_\infty$	free stream Mach number
$p$	pressure
$p_0$	local mean flow pressure
$p'$	sound pressure
$Q_i$	aeracoustic source term
$r$	distance from the source
$Re$	Reynolds number
$S_{ref}$	wing reference area
$t$	time
$\Delta t$	time step
$T_{ij}$	Lighthill stress tensor
$u_\infty$	velocity outside the profile boundary layer

$v$	velocity
$v_0$	local mean flow velocity
$v_{jet}$	jet velocity
$v_\infty$	free stream velocity
$\Delta x$	grid size

### Greek Symbols

$\alpha$	angle of attack
$\alpha_{max}$	stall angle
$\delta$	flap deflection angle
$\delta_0$	boundary layer thickness
$\delta_2$	momentum thickness of boundary layer
$\delta_{ij}$	Kronecker delta
$\varepsilon$	dissipation rate
$\zeta$	enstrophy
$\Theta$	directivity angle
$\lambda$	wavelength
$\lambda_f$	Taylor microscale
$\nu$	kinematic viscosity
$\Pi(x)$	indication parameter for whether position $x$ is in acoustic nearfield
$\rho$	density
$\rho_0$	local mean flow density
$\rho_\infty$	free-stream density
$\rho'$	(acoustic) density fluctuation
$\sigma$	relaxation parameter
$\tau_{ij}$	viscous stress tensor
$\vec{\omega}$	vorticity vector
$\Omega$	vorticity
$\Omega^{ref}$	target vorticity

### Indices

$dim$	dimensional quantity
$\infty$	free-stream quantity
$0$	mean flow quantity

### Acronyms

<i>APE</i>	<u>A</u> coustic <u>P</u> erturbation <u>E</u> quations
<i>AFC</i>	<u>A</u> ctive <u>F</u> low <u>C</u> ontrol
<i>CAA</i>	<u>C</u> omputational <u>A</u> eroacoustics
<i>CFD</i>	<u>C</u> omputational <u>F</u> luid <u>D</u> ynamics
<i>CFL</i>	<u>C</u> ourant- <u>F</u> riedrichs- <u>L</u> evi
<i>dB</i>	<u>d</u> ezi <u>B</u> el
<i>DES</i>	<u>D</u> etached <u>E</u> ddy <u>S</u> imulation
<i>DLR</i>	<u>D</u> eutsches Zentrum für <u>L</u> uft- und <u>R</u> aumfahrt (German Aerospace Center)

---

<i>DNS</i>	<u>D</u> irect <u>N</u> umerical <u>S</u> imulation
<i>fRPM</i>	<u>f</u> ast <u>R</u> andom <u>P</u> article <u>M</u> esh
<i>Hz</i>	<u>H</u> ertz
<i>ICAO</i>	<u>I</u> nternational <u>C</u> ivil <u>A</u> viation <u>O</u> rganization
<i>LEE</i>	<u>L</u> inearized <u>E</u> uler <u>E</u> quations
<i>Mic1</i>	<u>M</u> icrophone on circle <u>1</u> at distance 0.2m from trailing edge
<i>Mic2</i>	<u>M</u> icrophone on circle <u>2</u> at distance 0.3m from trailing edge
<i>OASPL</i>	<u>O</u> ver <u>a</u> ll <u>S</u> ound <u>P</u> ressure <u>L</u> evel
<i>PIANO</i>	<u>P</u> erturbation <u>I</u> nv <u>e</u> stigation of <u>A</u> erodynamic <u>N</u> oise
<i>PPW</i>	<u>P</u> oints <u>P</u> er <u>W</u> avelength
<i>RANS</i>	<u>R</u> eynolds- <u>a</u> veraged <u>N</u> avier- <u>S</u> tokes
<i>RPM</i>	<u>R</u> andom <u>P</u> article <u>M</u> esh
<i>SPL</i>	<u>S</u> ound <u>P</u> ressure <u>L</u> evel

# Chapter 1

## Introduction

Airplane noise emissions have shifted into focus in recent decades, as air traffic increased [1]. Excessive noise causes an annoyance to communities living near airports, especially as new housings are built even closer to these facilities [2]. Regulations are given in the ICAO Annex 16 Volume 1 to limit noise emissions [3]. In order to satisfy these new licensing criteria, research initially focused on the engines, as the emission from these airplane parts was most substantial[2]. An increased understanding of aeroacoustic source mechanisms in different parts of the engines, sound propagation and interaction with other parts of the airplane, as well as new liner technology allowed for a substantial reduction in engine noise emissions compared to previous engine models[2]. The trend towards higher bypass ratios has also lead to a substantial reduction of engine noise[2]. However, there are still other areas with great noise reduction potential.

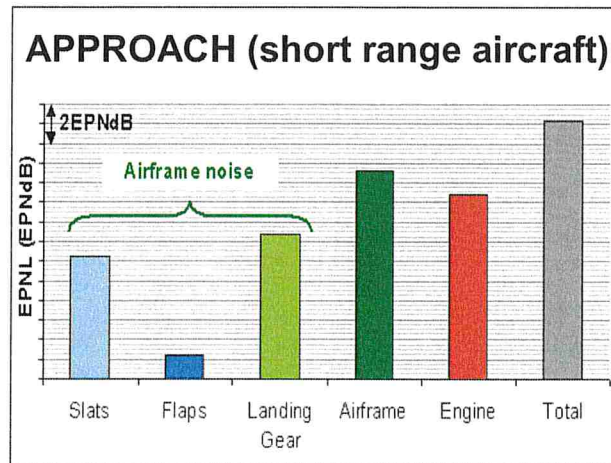


Figure 1.1: Component breakdown of noise contribution during approach for modern short to medium range transport aircraft from Airbus SILENCER project [4]

Figure 1.1 shows the noise contributions from different airplane components of a representative short- to medium-range transport aircraft during the approach phase[5]. This data stems from the Airbus SILENCER project [4]. As the figure shows, the engines are no longer the primary contributors, though their contribution is still significant. The noise produced by the airframe now exceeds engine noise. To achieve a reduction in overall aircraft noise at approach, it would now be necessary to first reduce the most dominant source followed by an equal reduction of all sources once the noise contributions are at similar levels[2]. It should also be mentioned that during take-off, engine noise is still dominant, meaning further reductions on this sound source are still necessary [2]. The category of airframe noise is dominated by the sound produced by

the landing gear as well as the high lift system [2]. The noise produced by high lift systems originates mostly from the gaps in a common three-element slat-wing-flap configuration, with the slat contributing more significantly to the noise production than the flap [6].

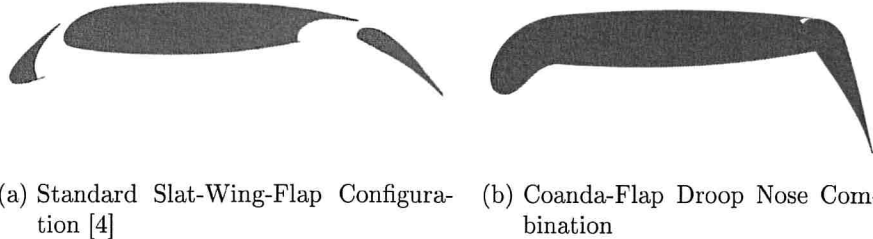
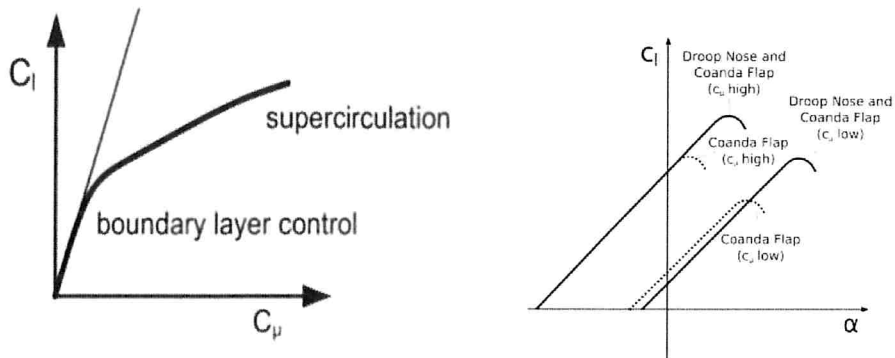


Figure 1.2: 3-Element-Wing vs. Gapless High Lift System

An effective way to reduce airframe noise in this area would be to move away from this configuration to a gapless high lift system [7]. One of the major reasons for the popularity of the slat-wing-flap system is a larger lift increase compared to most gapless systems [8]. Active Flow Control (AFC) offers a way to increase the high lift potential of a gapless system with a significantly smaller increase in noise emission [6]. A Coanda-flap combined with a droop nose would be one such a low-noise high-lift device [9]. The high-speed tangential jet blown across the flap increases the high lift potential proportionally to the blowing intensity [7]. This can be seen in figure 1.3a. The two different slopes are owed to different mechanisms of lift increase. The transition from boundary layer control to supercirculation occurs, when the flow is fully attached along the entire flap and the blowing momentum is increased further [10].



(a) Effect of Blowing Momentum on the Lift Coefficient [10]      (b) Example of Lift Curves for Coanda Flap Configurations [11]

Figure 1.3: Effect of Coanda Blowing Momentum on Generated Lift

The jet does increase the noise production compared to a gapless system without AFC [12], but the noise produced by the overall high lift system has been shown to be lower than is the case with a three-element wing [6]. In their 2010 publication [6], Pott-Pollenske and Pfingsten were able to show a noise reduction between 2 and 20 kHz, with an increase in noise for frequencies lower than 2 kHz. Both wind tunnel tests and two-dimensional aeroacoustic simulations have so far been conducted to locate sound sources on this system [13]. Sources were mostly located near the flap, where the jet interacts with the solid surface [13]. In an analytical study on the noise generated by a hydrofoil with a Coanda wall jet Circulation Control device [14], Howe identified 4 different source mechanisms present in a Coanda profile with a rounded trailing edge as the

Coanda surface. Applied to the present configuration, these mechanisms were reduced in [13] to three sources present on a Coanda flap.

- classic trailing edge noise on the flap trailing edge
- curvature noise at the rounded flap surface
- jet mixing noise

The analysis in [13] also showed that the latter of these three sources produces a higher frequency than the other two and noise from this source mainly radiates upward. This exempts jet mixing noise from this analysis, as the search is aimed at identifying which source would dominate the noise perceived on the ground. Jet mixing noise would be very much affected by shielding and atmospheric dampening, so it isn't likely to contribute much to the overall noise signal[13]. This only leaves trailing edge noise and curvature noise as contenders for the dominant sound source. As both these sources depend on turbulence interacting with geometry, the next step is to extend simulations into the third dimension to better resolve the three-dimensional turbulence and thus compare the noise production by these sources more accurately. These simulations will also show, whether the 2D simulations were able to capture the shape of the sound spectra accurately.

# Chapter 2

## Theory

### 2.1 High Lift Configurations

As the airfoils of modern airplanes are optimized to reduce drag under cruise conditions, they are unable to provide the high amount of lift at low speeds necessary for take-off and landing [10]. High lift devices on the leading and trailing edge of the wings can solve this problem. When deployed, they change the geometry of the wing to produce more lift, which simultaneously increases drag [15]. When the devices are retracted during cruise flight, they move back into position so that the original wing profile for low drag is achieved [15].

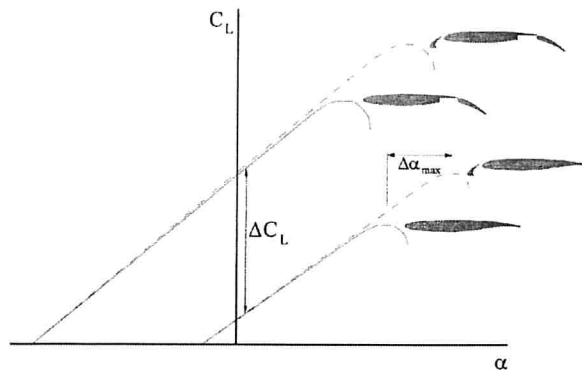


Figure 2.1: Effect of leading vs trailing edge devices on the lift curve [16]

Though both leading edge and trailing edge devices are aimed at providing a higher lift coefficient, they have different effects on the lift curve of the wing, as shown in figure 2.1 [16]. A leading edge device, such as the slat in the figure would serve to extend the lift curve towards higher stall angles as well as higher lift coefficients. As seen in the figure, a trailing edge device shifts the entire curve upwards, increasing the lift coefficient at every angle of attack. However, the figure also shows that the stall angle decreases if only a trailing edge device is applied. Thus, a combination of a trailing and a leading edge device is often favored, as the leading edge device not only increases the maximum lift coefficient further but also raises the stall angle, avoiding a reduction of the flight envelope [15].

High lift systems are further divided into passive and active systems [15]. "Passive high lift device" is a term that generally refers to the more conventional high lift systems, which rely on a modified wing geometry to achieve a higher lift coefficient [15]. An active high lift system on the other hand locally changes the energy of the flow, for example using a high-velocity jet to add to the energy of the flow or by boundary layer suction [15]. A conventional three-element

slat-wing-flap configuration would be part of the first category, as the fast stream through the slot is produced only by the geometry and energy is neither injected nor extracted [17].

This thesis deals with the combined high lift system of a Coanda flap on the trailing edge and a simple droop nose on the leading edge. The focus of this thesis will be the Coanda flap, which is considered an active device [15]. The droop nose, which is classified as a passive device, replaces the slat at the leading edge [15]. A droop nose has a similar effect on the lift curve as the slat, though its high lift potential is lower [15]. The smooth contour of the droop nose is very beneficial for noise reduction and it counteracts the stall angle reduction that a Coanda flap would produce. The Coanda flap is required to generate a comparable or higher lift than the slat-wing-flap configuration. It also generates the majority of noise produced by this high lift configuration, making it the focus of this analysis [6].

### 2.1.1 The Coanda Flap

A Coanda flap consists of a plain flap with the addition of a small blowing slot from which a thin jet is driven across the surface of the flap [10]. The Coanda effect, discovered by Henri Coanda in 1910 [18], causes the jet stream to follow the curvature of the so-called Coanda surface and the surrounding air to be entrained by the jet. This helps to delay flow separation on the flap and allows for a higher flap deflection angle, thus increasing the lift yield [10]. The relevant flow regions are schematically shown in figure 2.2. Blowing intensity is commonly quantified by the momentum coefficient  $C_\mu$  and the lift gain is proportional to it [10] as was shown in figure 1.3a.

$$C_\mu = \frac{\dot{m} \cdot v_{jet}}{\frac{1}{2} \cdot \rho_\infty \cdot v_\infty^2 \cdot S_{ref}} \quad (2.1)$$

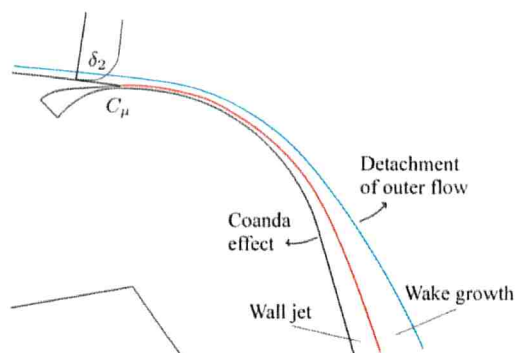


Figure 2.2: Coanda effect on Coanda flap [10]

## 2.2 Aeroacoustic Sources

The field of aeroacoustics considers flow-induced sound generation, as well as the propagation of sound waves through a moving medium [19]. Acoustic signals can generally be divided into tonal and broadband noise, though most signal will be a mixture of both with either tonal or broadband components being dominant [19]. One example of tonal noise would be the complex tone produced by a propeller[20]. The corresponding blade passing frequencies can be seen in the sound spectrum (figure 2.3) as peaks with decreasing sound pressure level as the frequency of the tones increases [20]. The blade profiles themselves also produce a broadband signal as they are passed over by a turbulent flow [20]. This mechanism is commonly referred to as "self noise" [21]. It is reflected in the spectrum by the sound pressure levels of frequencies between the distinct peaks [20].



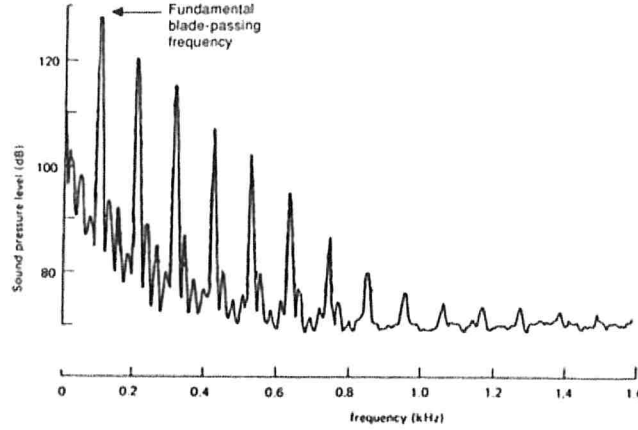


Figure 2.3: Sound spectrum of propeller noise [20]

The first attempt at understanding the generation of sound in turbulent flows was made by Sir Michael James Lighthill in 1951 [22]. He transformed the nonlinear Navier Stokes equations to arrive at the shape of an inhomogeneous wave equation. All terms remaining on the opposite side of the wave operator were interpreted as aeroacoustic sources.

$$\frac{\partial^2 \rho'}{\partial t^2} - a_\infty^2 \Delta \rho' = \frac{\partial^2 T_{ij}}{\partial x_i \partial x_j} \quad (2.2)$$

$$T_{ij} = \rho v_i v_j - \tau_{ij} + \delta_{ij}(p' - a_\infty^2 \rho') \quad (2.3)$$

Equation 2.2 is known as Lighthill's aeroacoustic analogy and the term  $T_{ij}$  is coined the Lighthill stress tensor. The second derivative of this tensor results in a quadrupole source [23]. This equation was derived directly from the nonlinear Navier Stokes equations without any approximations or simplifications. It is universally applicable [23]. The underlying mechanisms of sound generation and sound propagation were not taken into account, however, which resulted in some propagation mechanisms being included as sources[23]. This is mostly owed to the fact that the linear wave operator on the left-hand side of the equation assumes no background flow, which would influence the wave propagation [23]. Another shortcoming of the equation is, that it cannot take into account, how acoustic pressure fluctuations can interact with flow and thus change sound sources, creating a feedback loop. A common example of this kind of feedback is the so-called cavity flow [24]. The shear layer over a cavity produces sound, which is reflected at the opposite corner of the cavity and thus propagates upstream, where it destabilizes the shear layer and changes the sound source [24].

Lighthill's analogy is most commonly applied for jet noise which is dominated by the sound produced by free turbulence [23]. The large Lighthill stresses within the turbulent shear layer of a cold jet produce sound that is related to the time between two neighbouring vortices passing the same point in space [23]. The most dominant parameters in this case are the jet diameter and the velocity of the turbulent flow[23]. A common approximation for the sound intensity of jet noise is provided by equation 2.4 [23].

$$\langle \rho'^2 \rangle \sim \rho_0^2 M^8 \frac{D^2}{r^2} \quad (2.4)$$

This 8th power-law only applies for small Mach numbers  $M \ll 1$ , cold jets and a uniform density  $\rho_0$  and has been experimentally proven for this specific case[23].

At high Reynolds and low Mach numbers, as well as a constant density, the second spatial derivative of the Lighthill stress tensor can be approximated in the far-field according to equation 2.5 [23].

$$\frac{\partial^2 T_{ij}}{\partial x_i \partial x_j} = \rho_0 \frac{\partial^2 v_i v_j}{\partial x_i \partial x_j} = \rho_0 \nabla (\vec{\omega} \times \vec{v}) \quad (2.5)$$

The variable  $\vec{\omega}$  represents the vorticity of a vortex, which would be equal to zero everywhere, except at the core of the vortex itself [23].  $\vec{v}$  denotes the velocity with which the vortex is convected through the flow. In order for the divergence of  $\vec{\omega} \times \vec{v}$  to be non-zero, and thus sound to be produced, the product of the vorticity  $\vec{\omega}$  and the convective velocity  $\vec{v}$  would need to fluctuate in time [23]. An irrotational vortex with constant vorticity can only produce sound, if it is subjected to an acceleration resulting in a change in the convective velocity  $\vec{v}$  over time [23]. A single vortex would only emit sound in a dipole pattern. Only the interaction of two vortices creates the typical quadrupole sound radiation, as the two dipoles are superpositioned [23].

Generally, it can be said, that whenever a turbulent flow is subjected to an acceleration, it will produce broadband noise [23]. The two aeroacoustic source mechanisms discussed in this thesis are trailing edge and curvature noise. Both these sources are mainly based on the acceleration of turbulent flow due to an adjacent geometry and thus produce broadband, rather than tonal, noise.

Only frequencies below 30 kHz will be considered relevant for this analysis, as atmospheric absorption affects higher frequencies to a larger degree, diminishing their impact on noise detected at ground level. The simulation model is about  $\frac{1}{10}$  the size of the full-size wing and the Helmholtz numbers (see section 2.3) are identical. This means that the frequencies measured in the simulation are 10 times higher than they would be in case of the full-size aircraft. A frequency of 30 kHz would thus be equal to 3 kHz. The atmospheric dampening at 3 kHz would reduce sound pressure levels by nearly 5 dB per 100 m at low humidity and 1.5 dB at very high humidity. A higher frequency such as 4 kHz would experience an absorption of 7.5 dB per 100 m at low humidity and 2.1 dB at high humidity.

### 2.2.1 Trailing Edge Noise

Trailing edge noise is caused by a turbulent flow moving across the sharp trailing edge of a geometry [25]. The turbulence kinetic energy contained in the turbulent eddies is scattered into sound as they cross the edge, producing a broadband signal. The characteristic frequency produced by a vortex moving across a sharp trailing edge is proportional to the size of the vortex as well as its velocity [26]. Trailing edge noise is only produced in the duration of the vortex moving across the edge [26].

$$I_{3D} \simeq \frac{\overline{p'^2}}{\rho_\infty a_\infty} \sim v_0^3 M_0^2 \frac{b \delta_0}{r^2} [5] \quad (2.6)$$

Equation 2.6 shows some influencing parameters on the sound intensity of trailing edge noise [5]. The flow velocity  $v_0$  and  $M_0 = \frac{v_0}{a_\infty}$  represents an important factor in the amplitude of trailing edge noise, as it follows a fifth power law [2]. The sound intensity also scales with distance  $r$  from the source, the span  $b$  of the trailing edge, as well as the boundary layer thickness  $\delta_0$  which is a measure of the size of the largest eddies in the turbulent boundary layer. For subsonic cases, as the sound intensity of free turbulence jet noise scales with flow Mach number to the power of 8, trailing edge noise, which scales with a fifth power law, will always be dominant [27].

Common ways to reduce trailing edge noise are a backward swept or serrated trailing edge, which reduces the flow velocity normal to the edge, as well as the application of brushes to the trailing

edge or porous trailing edges to allow for an equalization of pressure and reduce trailing edge scattering [2] [5].

### 2.2.2 Curvature Noise

In [14] Howe refers to the sound produced by a turbulent boundary layer flow moving along the rounded edge of a geometry as "curvature noise". This bears resemblance to trailing edge noise, as the sound is produced by the interaction of a turbulent flow with a specific geometry. Applied to the case of a Coanda flap, the boundary layer flow would be replaced with the tangentially blown wall jet across the curved Coanda surface. As the jet would be of higher velocity than the external flow and the sound generation by turbulence-geometry interaction increases with the velocity of the turbulent flow, a significant noise contribution is to be expected from this source. Additionally, the interaction of a turbulent vortex with the geometry of the flap curve would be of longer duration than is the case at the flap trailing edge. The boundary layer is however significantly thinner at the flap shoulder, where curvature noise occurs, than at the trailing edge. This difference in  $\delta_0$  results in smaller eddies and reduces the sound intensity of curvature noise. Depending on the microphone position, the distance  $r$  may also be larger for curvature noise. This difference would, however, become diminishingly small in the far-field.

## 2.3 Acoustic far-field vs. near-field

The acoustic pressure field is generally split for the purpose of analysis into two areas; the acoustic near-field and far-field. This division of the sound field allows for different simplifications and assumptions to be applied to each area, as acoustic waves behave differently in close proximity to the source compared to far away from it [19]. These simplifications provide less complex equations, that are easier to solve for each area [19].

The pressure signal in the acoustic near-field of a source behaves as though it propagates through an incompressible medium [19]. It does not move with the speed of sound, therefore the signal cannot be considered as sound, but is instead governed by hydrodynamic principles [19]. The amplitude decay in the near-field is proportional to  $\sim \frac{1}{r^2}$  and thus much faster than in the far-field, where it follows  $\sim \frac{1}{r}$  [19]. In the far-field, compressibility effects take hold, the disturbances move as acoustic waves and can be registered as sound signals [19].

To determine, where the acoustic near-field ends and the far-field begins, the distance from the source is compared to the acoustic wavelength of the signal. The acoustic near-field is active in the area where the distance from a point source is significantly smaller than the acoustic wavelength of the signal it generates [19]. As the distance is increased to one acoustic wavelength and beyond, compressibility effects start to influence the signal and the acoustic far-field is reached [19].

Another influencing factor is the compactness of the source. It can be expressed using a dimensionless parameter called the "Helmholtz number"  $He$ . The Helmholtz number compares the size of the source  $l_S$  to the acoustic wavelength  $\lambda$  [19]. A source that is significantly smaller than the acoustic wavelength would be considered compact, marked by  $He \ll 1$  [19]. In practical applications, a value of  $He = 0.25$  would still be considered a compact source [19]. When the scale of the source is equal to or larger than the acoustic wavelength, it would be considered non-compact [19].

The compactness of a source can impact the pressure field and the boundary between near-field and far-field significantly. A non-compact source will produce no true acoustic near-field in the region where  $d_S \ll \lambda$  [19], as the large extension of the source prevents this. Instead, a geometric near-field will form, where both hydrodynamic and acoustic processes take place [19]. A similar distinction can be made for the far-field. The geometric far-field would begin

at a distance that is significantly larger than the extension of the source  $d_S \gg l_S$  [19]. The acoustic far-field, however, begins as soon as the distance is no longer smaller than the acoustic wavelength, independently of the source extension [19].

When an obstacle is present in the sound field of a source, the area surrounding that obstacle also becomes a near-field as the reflection of sound on the surface of the obstacle is modeled as an additional source [19].

$$\Pi(x) = \max \left[ \frac{d_S(x) + l_S}{\lambda}, \frac{d_B(x) + l_B}{\lambda} \right] = \max \left[ \frac{d_S(x)}{\lambda} + He_S, \frac{d_B(x)}{\lambda} + He_B \right] \quad (2.7)$$

Equation 2.7 provides a method for determining, whether a specific position  $x$  is located in the acoustic near-field or far-field. In the acoustic near-field  $\Pi(x)$  would be significantly smaller than one, which the large Helmholtz number of a non-compact source would prevent [19]. The equation also considers the presence of a body at a distance  $d_B(x)$  and of size  $l_B$ . The overlap of the acoustic far-field from that body ( $\frac{d_B(x)+l_B}{\lambda} > 1$ ) can also prevent a purely hydrodynamic near-field around the source [19].

For broadband sources, the characteristic wavelength is determined by identifying the most dominant frequency within the spectrum of the source in a specific direction. In [28], the amplitude decay of the sound emitted by a trailing edge source is recorded in the radiation direction towards the ground. It was observed that the decay followed the typical near-field proportionality up to a distance of 1.2 chord lengths from the source. The microphone positions within the present work, which will be explained within the following chapter, would not be part of the far-field, according to this approximation. The recorded data will thus be near-field data only.

# Chapter 3

## Numerical Method

### 3.1 Computational Aeroacoustics

Computational Aeroacoustics or CAA, compared to general Computational Fluid Dynamics, is a relatively new field, depicting and analyzing the sound generated by flows, the sound propagation through flows, as well as interactions between sound and flow (i.e. cavity noise). An important feature of CAA is the ability to consider gradients in the flow, which is hard to accomplish using analytical methods. As these gradients strongly impact sound propagation, contribute to the noise signal and are very nearly omnipresent in all technical applications of flow, CAA plays an important role in current aeroacoustic research.

In Computational Aeroacoustics the governing equations of aeroacoustics, e.g. the Linearized Euler Equations (LEE), the Acoustic Perturbation Equations (APE) or other nonlinear equations [29], are solved numerically on a computational grid for volume discretization in order to be able to predict sound propagation in non-uniform flows. In order to obtain the flow field, across which the sound would propagate, a CFD simulation needs to be conducted. The CFD and CAA simulations can be done either simultaneously or consecutively. For this examination, the two-step consecutive CFD-CAA-hybrid approach, which uses the fRPM method to synthesize turbulent structures from the statistical data of a steady Reynolds-averaged-Navier-Stokes (RANS) simulation, was chosen, as it presents the most time-efficient approach [30]. Other methods may use high fidelity CFD codes such as LES, DES or DNS to achieve great accuracy at significantly higher computational cost [31].

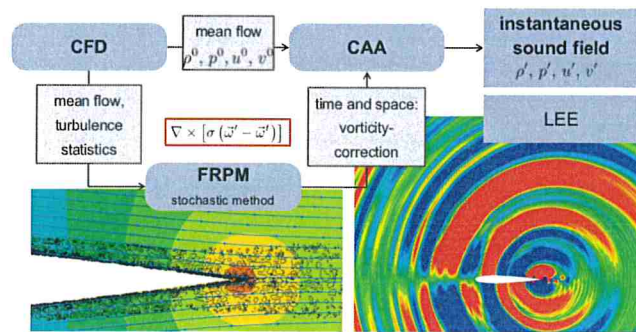


Figure 3.1: Schematic of CFD-CAA hybrid approach [13]

The unsteady Euler Equations are able to describe vorticity, entropy as well as acoustic modes [29]. The small magnitude of acoustic fluctuations compared to mean flow quantities allows for the use of the linearized equations [29].

Numerical schemes require high accuracy and low dispersive errors to be appropriate for CAA [26]. Acoustic boundary conditions must be well defined to avoid sound reflection on virtual boundaries of the computational domain [26].

Different discretization schemes employ various stencils. The stencil used in the numerical scheme has an impact on the required mesh resolution [26].

$$PPW = \frac{\lambda}{\Delta x} = \frac{a_\infty}{f \Delta x} \quad (3.1)$$

$$\Delta x \leq \frac{\lambda}{PPW} = \frac{a_\infty}{f \cdot PPW} \quad (3.2)$$

To determine the time resolution or time step size, the Courant-Friedrichs-Levi-Number (CFL)(equation 3.3) is used. In order to resolve acoustic signals using explicit schemes, a CFL number of 1 or less is necessary, with a number of exactly 1 being ideal [29]. This provides a direct correlation between the time step  $\Delta t$  and the grid resolution  $\Delta x$ . The velocity  $v$ , in this case, would be the speed of sound  $a$  added to the velocity of the flow. As a global timestep is used for the entire domain, the time step would be determined by the minimal ratio of  $\Delta x$  to  $v$ . Therefore, if there is a high resolution in areas of high flow velocities, these areas will be critical for determining the timestep.

$$CFL = \frac{v \Delta t}{\Delta x} \leq 1 \quad (3.3)$$

$$\Delta t \leq \frac{\Delta x}{v} \quad (3.4)$$

A larger time step is advantageous, as it reduces overall computation time, which is still a major issue in aeroacoustic simulations [29].

## 3.2 PIANO

The CAA Code PIANO is being developed by the DLR [32]. Its purpose is to simulate aeroacoustic noise generation and acoustic wave propagation through non-uniform flows. PIANO stands for Perturbation Investigation of Aerodynamic Noise [32]. The PIANO Code supports the Linearized Euler Equations (LEE), which were used in this analysis, the Acoustic Perturbation Equations (APE), as well as non-linear equations. The solver requires a block-structured, curvilinear mesh and relies on a fourth-order DRP scheme for spatial discretization as well as a fourth-order Runge-Kutta scheme for time. The numerical scheme uses a 7 point stencil, meaning the mesh must satisfy the criterium of 7 PPW. According to equation 3.2, to resolve a frequency of up to 30 kHz a mesh resolution that is finer than  $\Delta x = 0.00162$  would be required. The timestep, however, is determined by the minimal  $\Delta x$ . As mentioned in the previous chapter, a larger timestep is beneficial for keeping computation time manageable. Therefore, the largest acceptable  $\Delta x$  should be chosen whenever possible, especially in areas where the mean flow velocity is high. The mean flow is calculated in a steady CFD RANS simulation as input for CAA.

PIANO uses all variables in their non-dimensionalized form [32]. The necessary reference quantities are the characteristic length (in this case the chord length)  $L = c = 0.3$ , the ambient speed of sound  $a_\infty$  and the ambient density  $\rho_\infty$ . Thus, the variables used in the PIANO simulation are:

$$t = t_{dim} \frac{a_\infty}{L}, \quad x_i = \frac{x_{i,dim}}{L}, \quad \rho = \frac{\rho_{dim}}{\rho_\infty}, \quad \vec{v} = \frac{\vec{v}_{dim}}{a_\infty}, \quad p = \frac{p_{dim}}{\rho_\infty a_\infty^2} \quad (3.5)$$

The index  $dim$  denotes the dimensional quantities. In all of the following equations, the non-dimensionalized quantities are used. The maximum mesh resolution would thus be  $\frac{\Delta x}{L} = 0.0054$ .

The Linearized Euler Equations used in the PIANO Code are in the shape of equation 3.6.

$$\begin{aligned} \frac{\partial \rho'}{\partial t} + \vec{v}' \cdot \nabla \rho_0 + \vec{v}_0 \cdot \nabla \rho' + \nabla \cdot \vec{v}_0 \rho' + \nabla \cdot \vec{v}' \rho_0 &= 0 \\ \frac{\partial \vec{v}'}{\partial t} + \vec{v}' \cdot \nabla \vec{v}_0 + \vec{v}_0 \cdot \nabla \vec{v}' + \frac{1}{\rho_0} (\nabla p' + \rho' \vec{v}_0 \cdot \nabla \vec{v}_0) &= Q_i \\ \frac{\partial p'}{\partial t} + \vec{v}' \cdot \nabla p_0 + \vec{v}_0 \cdot \nabla p' + \kappa [\nabla \cdot \vec{v}_0 p' + \nabla \cdot \vec{v}' p_0] &= 0 \end{aligned} \quad (3.6)$$

### 3.3 fRPM

The fast random particle mesh method, or fRPM for short, is required to reconstruct the turbulent vortices of a flow and thus turbulence-induced sound sources [30]. This additional step is necessary, as the results of a Reynolds-averaged Navier-Stokes simulation only provide time-averaged information and turbulence statistics. The fast RPM method represents an alternative numerical discretization of the previous RPM method without changing the underlying mathematical model [30]. The standard RPM method places random particles on equidistant streamlines in the resolved source domain. The particles are convected with the RANS mean flow, spatially filtered along the streamline, weighted and finally distributed normal to the streamline onto the CAA mesh [30]. The fRPM discretization uses an auxiliary cartesian mesh to resolve the source region. This is useful for areas of recirculation in the source regions, as these would introduce closed streamlines in the traditional RPM approach and the small error, that would result from the spatial filtering along the slightly curved streamlines, is also eliminated [30]. The cartesian grid is placed in an area where a high turbulence intensity occurs close to changes in geometry, as this would be where an aeroacoustic source could be expected. The grid is then populated with a number of virtual particles larger than the number of grid points [30]. The statistical input from CFD-RANS is then used to predict the movement of these virtual particles, reconstructing the turbulent structures in the flow and synthesizing the instantaneous turbulent flow fields [30]. Once the stochastic sound source reconstruction has been completed, the 4D spatial and temporal vorticity source term provided by this method is fed into the Linearized Euler Equations for the CAA simulation [33].

The calculation requires the mean flow velocities in all three coordinate directions, the turbulence kinetic energy, and the turbulence length scale to be interpolated onto the auxiliary grid [30]. From the kinetic energy and the grid size, a variable called enstrophy is calculated. The enstrophy field is used for the turbulence reconstruction as it depicts the distribution of vorticity without its directional component [34]. The enstrophy is calculated using equation 3.7. This equation is based on the entropy of homogeneous turbulence  $\zeta = \frac{\varepsilon}{\nu}$  [35] and the longitudinal Taylor microscale  $\lambda_f^2 = 20 \frac{k\nu}{\varepsilon}$  [36] with  $\varepsilon$  being the dissipation rate,  $\nu$  being the kinematic viscosity and  $k$  being the turbulence kinetic energy. The relation between the Taylor microscale and the fRPM grid size is  $\Delta x = c_y \lambda_f$  with the scaling constant  $c_y = 2$  for the present case [34].

$$\zeta(k) = \frac{20k}{4\Delta x} \quad (3.7)$$

The eddy relaxation source model by Neifeld et al. [33] couples fRPM and CAA, by providing the source term  $Q_i$  on the right-hand side of equations 3.6. The statistically modeled vorticity provided by the fRPM method is used to adjust the numerically resolved vorticity with a relaxation parameter  $\sigma$ , in order to model the aeroacoustic source for propagation across the

computational domain within the CAA simulation [33]. The relaxation parameter  $\sigma$  helps to control the production and destruction of vortices in the modeling [33].

$$Q_i = -\varepsilon_{ijk} \frac{\partial}{\partial x_j} \left[ \sigma \left( \Omega'_k - \Omega_k^{ref} \right) \right] \quad (3.8)$$

Equation 3.8 shows the Eddy Relaxation source term  $Q_i$ .  $\varepsilon_{ijk}$  represents the Levi-Civita symbol.  $\Omega_k^{ref}$  is time-resolved target vorticity distribution provided by the fRPM method [33]. The calculated  $Q_i$  becomes the source term in equation 3.6.



## Chapter 4

# Numerical Setup

The model for this analysis is a circulation control airfoil with a droop nose based on the DLR's F16 wing profile with a chord length of 0.3 meters. The same 2D model has been used in previous investigations [13]. After the mesh adjustments described in section 5.1 however, the comparability to the results from previous investigations is lost, as the computational domain is reduced in size in order to reduce computation times of the 3D simulations and no longer reaches the far-field. The simulations can therefore only capture near-field data, while the previous investigation mainly evaluated data from virtual microphones placed in the acoustic far-field. As explained in section 2.3 acoustic characteristics are very different in the far-field compared to close to the source. The simulation results will therefore only be compared to one another.

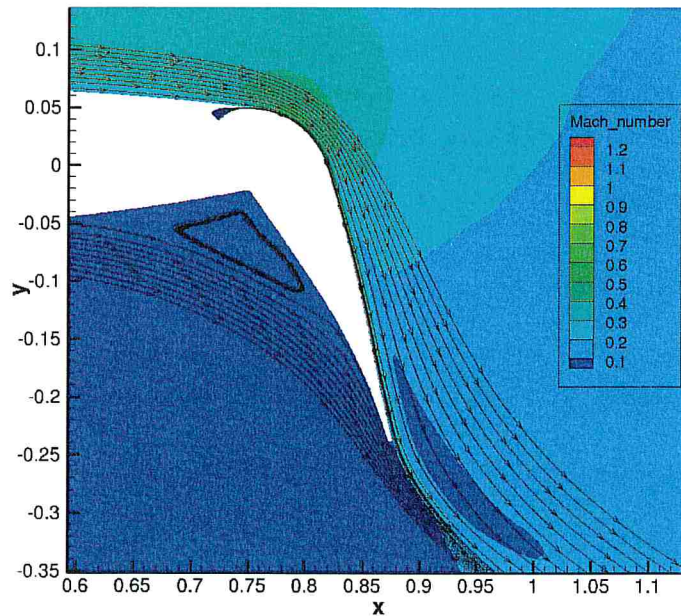


Figure 4.1: Mean Flow Field around Coanda Flap from CFD RANS

The flap deflection angle in the simulation is  $\delta = 65^\circ$ . From a 0.2 mm slot, the jet is blown at  $C_\mu = 0.056$ . This is sufficient to create a fully attached flow along the upper surface of the flap, as can be seen in figure 4.1. The figure shows the local mean flow Mach number in the vicinity of the flap. The streamlines show a fully attached flow down to the trailing edge. This mean flow data is attained from a steady RANS simulation completed prior to this analysis. As mentioned in the previous chapter, this mean flow serves as input for the CAA simulation. The free-stream Mach number is  $M_\infty = 0.151$  and the Reynolds number is  $Re = 1 \times 10^6$ .

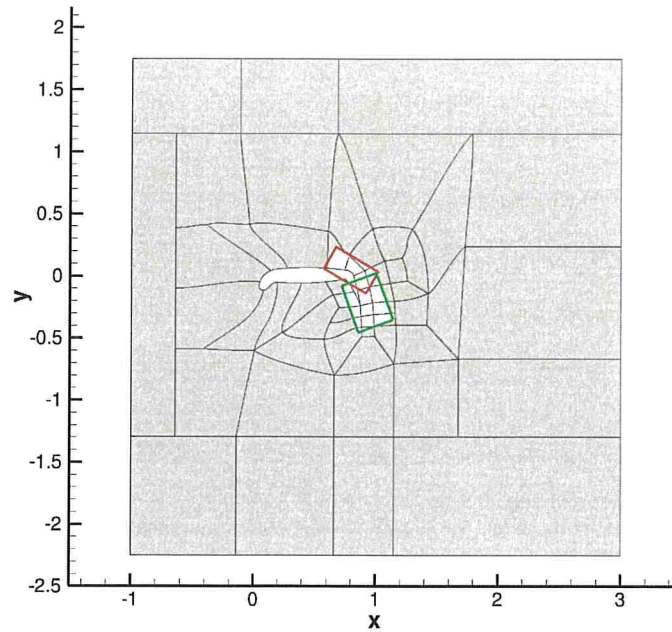
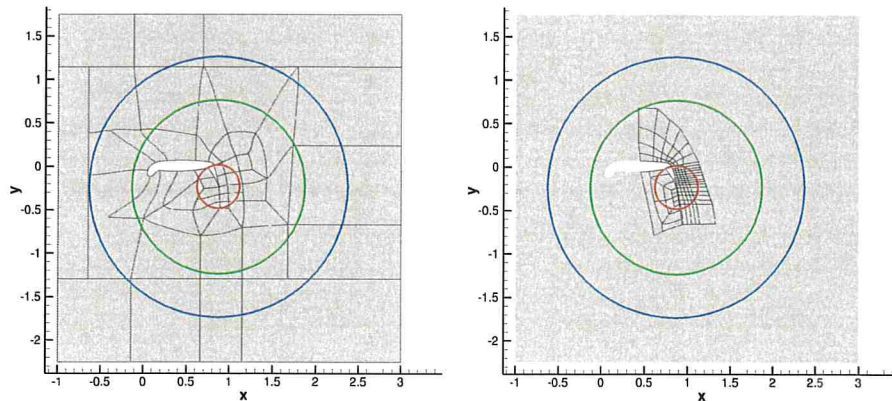


Figure 4.2: Starting 2D CAA mesh with trailing edge (green) and curvature (red) source region

Figure 4.2 shows the mesh as well as the areas for fRPM reconstruction at the start of this analysis. The mesh is identical to the previous 2D simulations in [13]. It is made up of 2.7 million cells. The grid size of both fRPM source regions is  $\Delta x = 0.0005$ . The mesh had to be reduced significantly in size and resolution for the three-dimensional simulations, as a simple 3D extrusion of the existing mesh would result in unacceptable computation times. The 3D simulations with the reduced mesh and a spanwise extension of merely than 1.2 % of the chord length required 3 weeks to complete.



(a) Microphone Circles in Previous Simulations (b) Previous Microphone Positions Compared to Size of New Grid

Figure 4.3: Comparison of Microphone Positions on top of Previous Mesh vs. New Mesh

Figure 4.3a shows the positioning of virtual microphones on the previous mesh. Microphones were placed on three circles centered around the trailing edge. The radius of the smallest was 0.25 m, the radius of the medium circle was 1 m and the largest circle had a radius of 1.5 m. Figure 4.3b shows an overlay of these microphone circles and the dimension of the new CAA mesh resulting from the preliminary simulations discussed in section 5.1. Only the smallest microphone circle would fit within the computational domain. Therefore, different virtual microphone positions

were chosen.

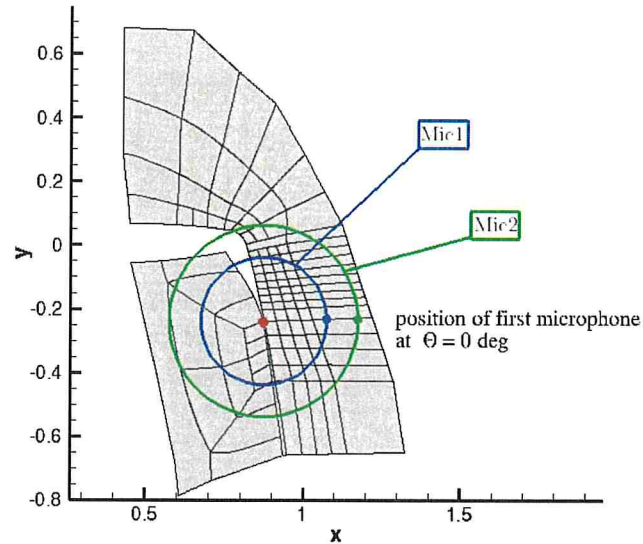


Figure 4.4: New positions of virtual microphone circles

The new microphone positions on top of the new mesh are shown in figure 4.4. The smaller circle with a radius of 0.2 m is subsequently referred to as "Mic1" and the larger, at a radius of 0.3 m is called "Mic2". The center of both circles is marked by the red dot. Along each circle, 360 microphones would be placed at an equal distance of  $1^\circ$ . The first microphone would be located at  $\Theta = 0^\circ$ , as marked in the figure. However, due to the small dimension of the computational domain, it was unavoidable, that both circles intersect the geometry, as well as the source region for curvature noise. The first will result in no microphones being placed in the area covered by the geometry. The second is likely to result in those microphones picking up large pressure fluctuations of not only acoustic but also vorticity modes.

# Chapter 5

## Results

The results of the aeroacoustic simulations are summarized and examined. The preliminary simulations aimed at reducing computation time by determining the minimum necessary extension and resolution of all relevant meshes will be explained first. The 2D and 3D simulation results, the application of a 2D-to-3D correction and a comparison of the sound spectra will follow.

### 5.1 Preliminary Simulations

As the main task of the thesis was to examine the aeroacoustic sources in three-dimensional simulations, the basic 2D mesh from previous studies needed to be optimized to provide all of the relevant information accurately while keeping the computation time as short as possible. This meant, that the resolution needed to be exactly at the limit of fulfilling all required criteria for resolving both the aeroacoustic sources and the acoustic wave signals. Additionally, it was examined, how far the computational domain had to extend, as this provided another way to reduce the number of cells in the mesh and thus computation time. Finally, the acoustic boundary conditions were tested on the two-dimensional mesh, before the first three-dimensional simulation could be started.

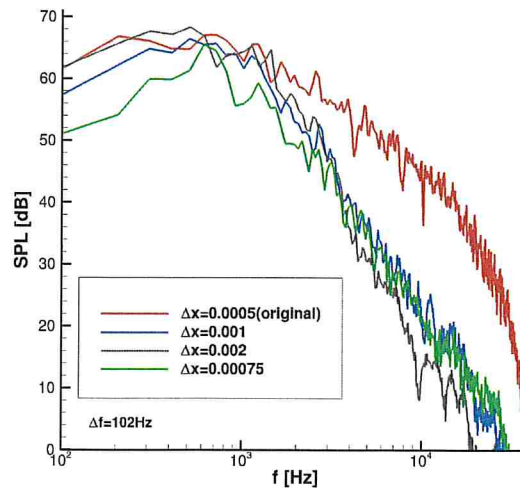


Figure 5.1: Narrow band spectra for different trailing edge fRPM meshes

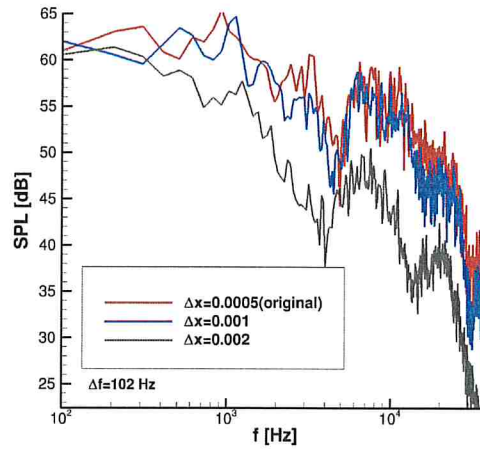
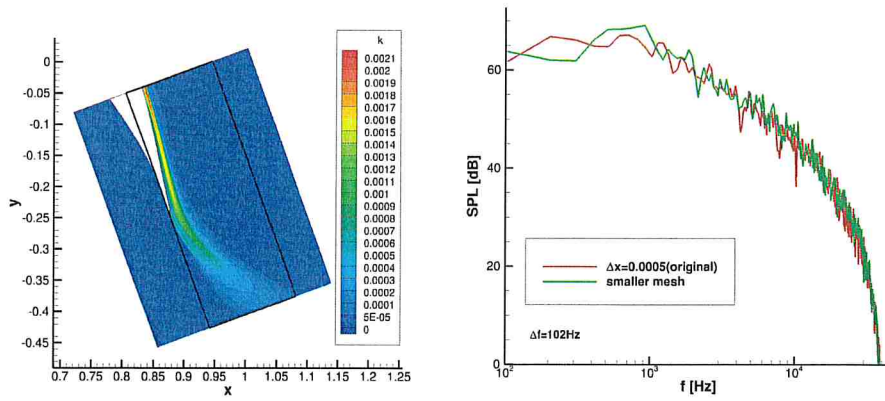


Figure 5.2: Narrow band spectra for different flap curve fRPM meshes

### 5.1.1 fRPM Meshes

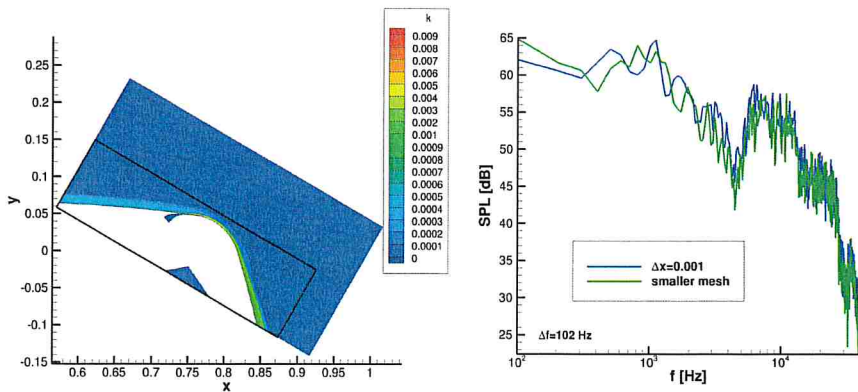
The fRPM method requires its own cartesian meshes and these meshes would also need to be extended into the third dimension. Their resolution also has a direct impact on the necessary resolution in areas of the acoustic mesh, as this mesh must be fine enough to resolve the turbulent structures reconstructed by the fRPM for the given source region. A first step was, therefore, to attempt a reduction of their resolution and extension and determine, whether the reduced fRPM still provided the same acoustic spectrum as the larger and finer mesh. The resolution was varied first. The original grid size of the fRPM mesh was  $\Delta x = 0.0005$ , corresponding to a minimum turbulent length scale of  $l_{min} = 4\Delta x = 0.002$  for the vortex reconstruction. For this examination, simulations with a fRPM grid size of  $\Delta x = 0.001$  and  $\Delta x = 0.002$  were run using the original acoustic mesh and the resulting pressure levels were compared to those from simulations using the original fRPM grid. These grid sizes correspond to minimum turbulent length scales of  $l_{min} = 4\Delta x = 0.004$  and  $l_{min} = 0.008$ . The comparisons are shown in figures 5.1 and 5.2. Figure 5.1 shows the pressure levels for the trailing edge noise. The difference in pressure levels is significant, even at a resolution of  $\Delta x = 0.001$ . A resolution of  $\Delta x = 0.00075$  was tested additionally, but even in this case, the pressure levels at frequencies above 2 kHz were significantly lower than in the original. It was therefore decided that maintaining the original resolution for the trailing edge noise source was the best option. It is possible, to draw conclusions about the nature of the trailing edge source from this result. The sound produced by small vortices with a length scale that is below  $l_{min} = 4 \cdot 0.00075 = 0.003$ , as would be present in close proximity to the wall within the remains of the jet flow, appears to be of great relevance for the trailing edge noise spectrum. As smaller vortices are often associated with the higher frequencies within the sound spectrum, this would lead to the sharp decline in the spectrum, as these vortices are no longer reconstructed by the fRPM method. On the other hand, figure 5.2 shows the results for the simulations for curvature noise. Here, a resolution of 0.001 still provides results that are reasonably close to the original. A resolution of 0.001 was thus chosen for the curvature source region. This result indicates, that for the curvature noise source, larger vortices between length scales of  $l_{min} = 0.004$  and  $l_{min} = 0.008$  are of higher relevance. This would mean, that the smaller vortices within the jet may contribute less to the sound generation by this aeroacoustic source.



(a) Area of smaller trailing edge fRPM (b) Comparison of narrow band spectra

Figure 5.3: Comparison of smaller trailing edge fRPM to original fRPM

Next, the scale of the fRPM meshes was reduced to only the areas, where the turbulence kinetic energy was high enough to contribute significantly to the aeroacoustic source. Whether this reduction was permissible was determined by the same method as in the previous investigation on the resolution. Figure 5.3a shows the previous and the reduced area of the trailing edge fRPM mesh and figure 5.3b shows the resulting pressure levels. As the pressure levels were in good alignment, the smaller mesh was chosen for the following 3D simulations. The pressure side being less relevant for the trailing edge noise source was suggested in [13], as near-wall velocities and thus turbulence levels on this side were low. Figure 5.3a reflects this as well, as the turbulence kinetic energy on the pressure side is clearly lower than on the suction side. The curvature noise mesh was adjusted similarly. The different meshes and the resulting pressure levels for this aeroacoustic source are shown in figure 5.4a and 5.4b respectively. The mesh extension was adjusted to include all areas of significant turbulence kinetic energy. The turbulence in the oncoming flow along the main wing suction side was also relevant for this source.



(a) Area of smaller flap curve fRPM (b) Comparison of narrow band spectra

Figure 5.4: Comparison of smaller flap curve fRPM to original mesh with 0.001 resolution

### 5.1.2 PIANO Grid

The main CAA grid was examined once the final fRPM meshes had been constructed. The grid shown in figure 4.2 was used in previous 2D aeroacoustic simulations conducted at the DLR [13]. The mesh consists of 2.7 million cells, which would multiply by the number of points by which the mesh is extruded in the third dimension. As this would lead to excessive computation times, a significant reduction was necessary.

The simulation time step is directly determined via the CFL number, as explained in chapter 3.1. The smallest grid size within this mesh thus also plays a vital role in terms of keeping computation time manageable. The resolution directly at the Coanda jet was very fine in this mesh, as it was previously also used to examine jet mixing noise from the Coanda jet as well as various momentum coefficients and thus required a higher resolution for the simulations to remain stable. The resolution did not need to be as fine in this simulation, as a constant momentum coefficient of  $C_\mu = 0.056$  was used for all simulations and jet mixing noise had already been excluded as it wasn't relevant for the noise perceived at ground level. The resolution at the jet exit was reduced iteratively to arrive at the minimum resolution at which the simulation would remain stable. This area was critical, as the jet velocity directly at the slot is the highest in the entire flow field. A high resolution of the jet would, therefore, reduce the available time step severely. Figure 5.5a shows the resolution at the jet prior to the modifications. The jet height was resolved by 20 points. This number was first halved and then further reduced to the final resolution of 6 points across the slot. By this method alone, the available timestep was raised from  $2.16\text{E-}5$  to  $8.12\text{E-}5$ , achieving an increase by a factor of 4. Figure 5.5b shows the resolution of the jet in the final mesh. The cells were stretched significantly to further reduce the number of points, as well as the necessary time step.

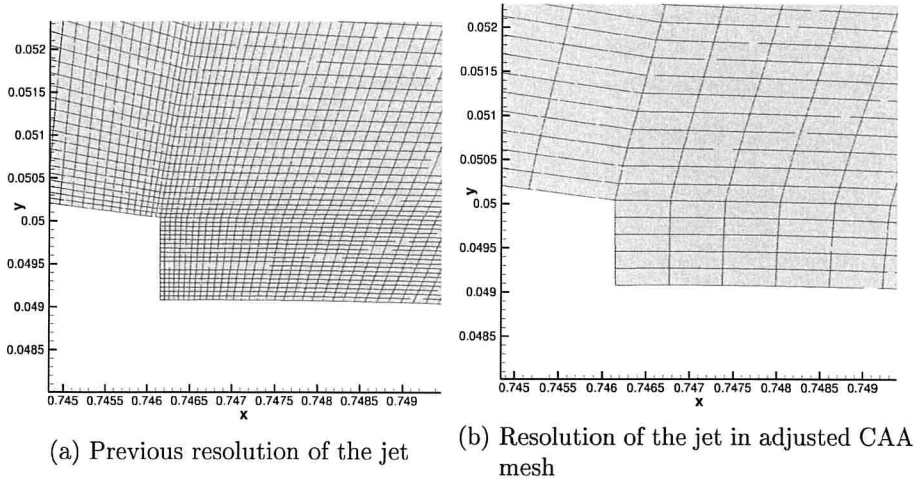


Figure 5.5: Comparison of jet resolution

The previously optimized resolution of the fRPM also affected the main CAA grid, as the resolution of the main mesh needed to be equal to or higher than the resolution of the fRPM in areas where they overlapped. While keeping this in mind, the resolution in all other areas of the mesh was reduced as much as possible without breaking the necessary condition, that the acoustic wavelength is resolved by at least 7 grid points. Using equation 3.2 the maximum grid size was calculated to be 0.0054 for a frequency of 30 kHz.

As for the area that needed to be covered by the computational grid, figure 5.6 shows the configuration that was determined to be sufficient. The area was just large enough, to encompass the relevant source regions and geometry and bring enough distance between these and the virtual boundaries to avoid issues with the boundary conditions. The domain no longer extended

into the far-field, making any comparison to results from wind tunnel tests no longer feasible. However, since the goal of this study was to determine the dominant aeroacoustic source based on comparing these simulations only to each other and this was possible using only near-field data, this expense was accepted. Figure 5.6 also shows the final CAA mesh with the areas for the new fRPM. This mesh consists of 674,153 cells with a grid size of  $\Delta x \leq 0.0054$ . The fRPM for the trailing edge consists of 240,000 and the fRPM for curvature noise of 44,000 cells.

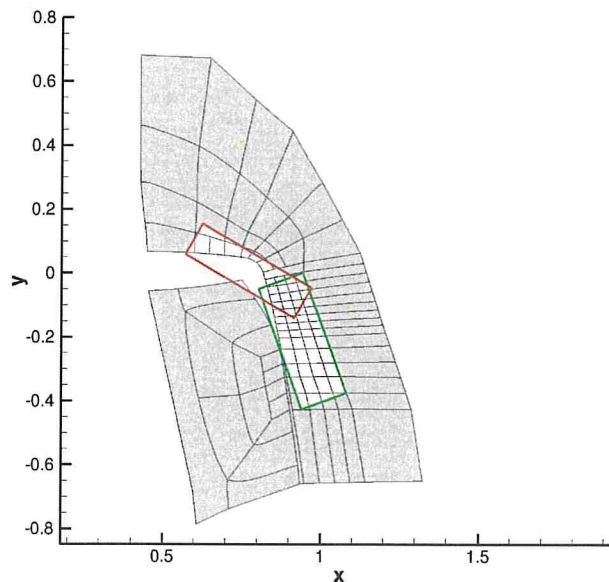


Figure 5.6: Blocks of new 2D CAA mesh with new trailing edge(green) and curvature(red) source regions

### 5.1.3 Boundary Conditions

The boundary conditions were chosen based on previous similar simulations. All boundaries on the surface of the geometry were set as acoustically no-slip walls. This boundary condition sets the mean flow as well as the fluctuating velocities to zero at the wall [32]. The same boundary condition was used for the jet exit, as the nearly sonic conditions at the nozzle, as well as the small diameter of the exit compared to the acoustic wavelength, prevent sound from propagating through this boundary, causing it to act similar to a wall from an acoustic perspective. The boundaries in spanwise direction in the 3D simulations were set as periodic boundaries. All remaining virtual boundaries of the computational domain were set as radiation boundaries.

Figure 5.7 shows the result of a 2D simulation for curvature noise. The pressure levels are adjusted to show vorticity modes, rather than acoustic modes. An interaction of these turbulent modes with the boundary can be seen at the bottom right corner of the computational domain. This indicates that rather than the modes simply exiting the domain there, they were being reflected by the specific boundary condition. The boundary condition in that corner was therefore changed from "radiation" to "outflow", which erased this interaction and lead to more accurate results.



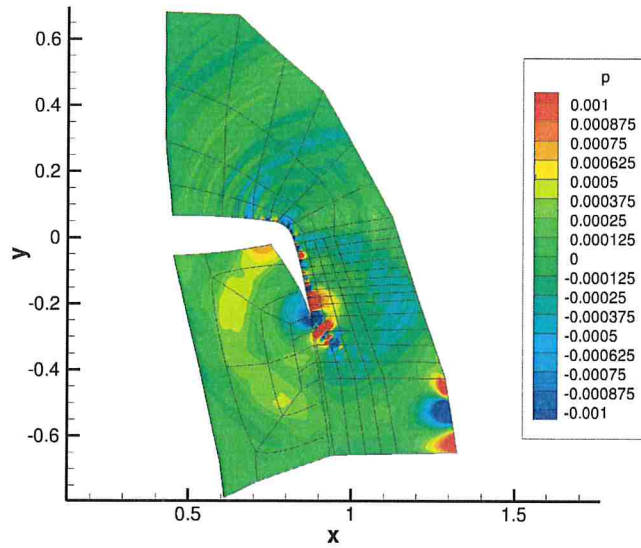


Figure 5.7: Reflection of turbulent vortices at radiation boundary

#### 5.1.4 Simulation results of final 2D mesh

With the finished 2D mesh and simulation setup, a simulation was done for each sound source. The resulting sound fields are shown in figure 5.8. These pressure fields show no more unwanted reflections. In the subsequent chapters, the extrusion of this grid in spanwise direction will be explained and the sound spectra recorded on the virtual microphones will be compared to the spectra extracted from these 2D simulations.

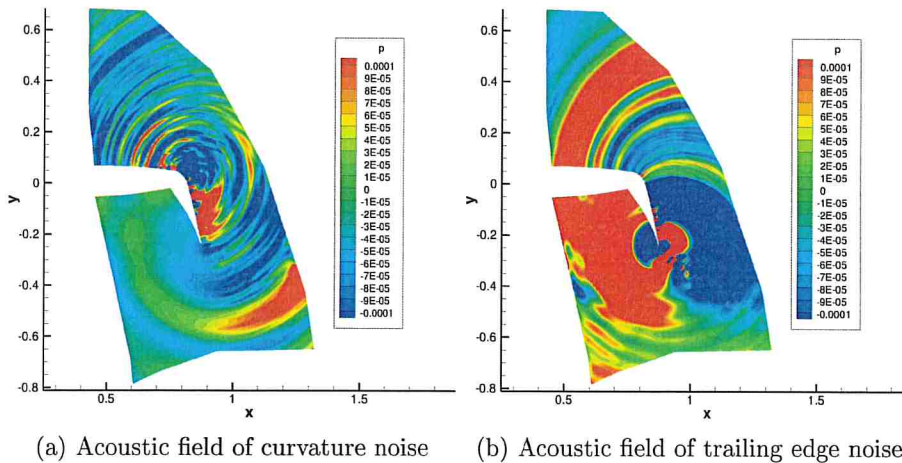


Figure 5.8: Acoustic fields from 2D simulations

## 5.2 3D Extrusion

Once the preliminary two-dimensional simulations were finished, the simulation could be extended to 3D. Both the main grid and the two fRPM needed to be extruded in spanwise direction. One requirement for the main grid was a resolution that was equal to or higher than that of the fRPM. As these meshes were equidistant cartesian grids, a spanwise resolution of  $\Delta x = 0.0005$

was necessary for both the main grid and the trailing edge mesh. The curvature fRPM had a new resolution of  $\Delta x = 0.001$ . This mesh therefore required about half as many points in spanwise direction at the same spanwise extension. The acoustic mesh with a finer spanwise resolution was used for both simulations to ensure comparability of the results to one another.

There were several criteria for the minimum extrusion of the mesh. The main grid was required to have at least 7 points in spanwise direction for the 7 point stencil of the numerical scheme. In order to fully resolve the turbulent vortices, the extension of the mesh in spanwise direction needed to be equal to the size of the largest eddies. Figure 5.9 shows the velocity profile extracted at the flap trailing edge, where the maximum boundary layer thickness is to be expected. In conventional boundary layer flows, the largest eddies can be approximated by the boundary layer thickness, which would be represented by the wall distance, where the external flow velocity  $u_\infty$  is reached. In this case, however, due to the jet, the largest eddies would likely be present between a wall distance of 0.008 and 0.03 in the remaining boundary layer separate from the eddies within the jet. These eddies are however not likely to be dominant in the sound signal, as the flow velocity in this region is significantly lower than in the jet. The jet height might, therefore, represent a better approximation for the size of the largest relevant vortices for the sound source. From the velocity profile, that height can be extracted as approximately 0.008 m, which would result in a dimensionless spanwise extension of the computational grid of  $\frac{l}{c} = 0.026$ .

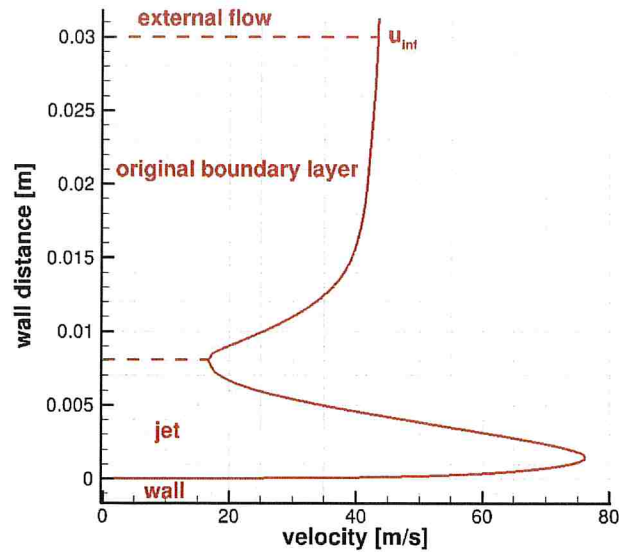


Figure 5.9: Velocity Profile of Mean Flow Extracted at the Flap Trailing Edge

Simulations were run with a spanwise extension of 0.006, 0.009 and 0.012 respectively. These simulations were able to finish within 3 weeks. Simulations with an extension of 0.014 did not finish in time for the evaluation. These simulations only completed 120,000 time steps within the first week. They would, therefore, take more than 1 month(4-5 weeks) to complete all 520,000 time steps required to capture the full acoustic signal. No further extensions of the mesh were attempted. The results of the remaining simulations will be discussed in the following chapters.

### 5.3 Effect of Spanwise Extension on Sound Pressure Levels

In this section, the simulation results in terms of sound pressure levels are compared, in order to ascertain, how the 3D extension of the computation affects the sound spectra. The directivities are compared and discrete microphone positions are selected for the comparison of sound spectra. In section 5.3.3, different corrections are applied to the sound pressure levels from the 2D simulations, to better match the 3D results.

#### 5.3.1 Trailing Edge Source

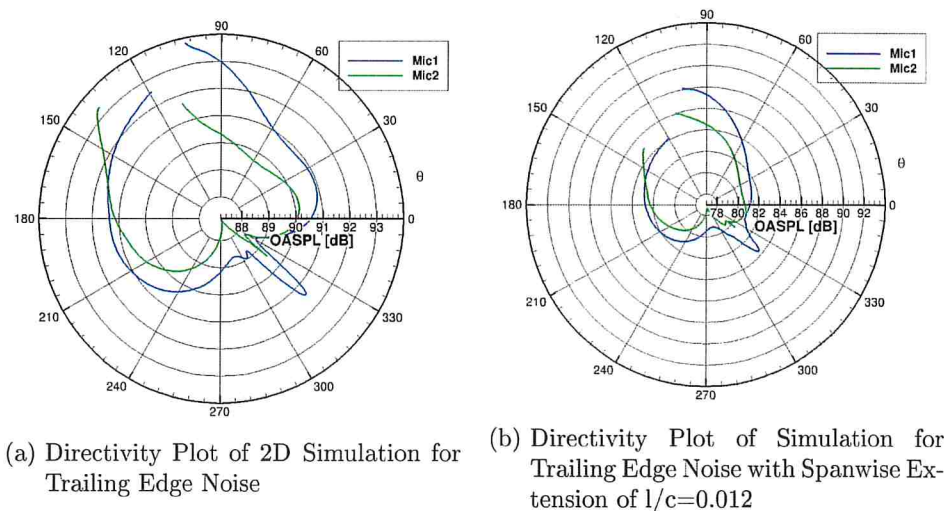


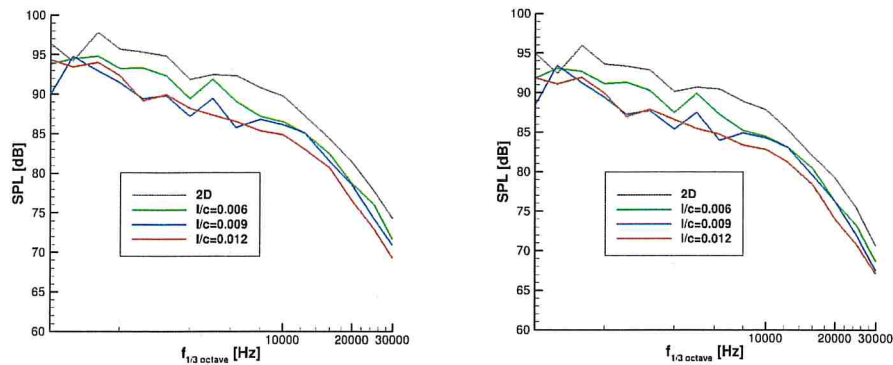
Figure 5.10: Directivity Plots for Trailing Edge Noise for 2D and largest 3D Extension

Figure 5.10 shows a comparison between the directivities extracted from the 2D and the largest 3D simulation. Mic1 refers to the smaller circle of microphones around the trailing edge, Mic2 refers to the microphone circle with a larger radius. The overall sound pressure level or OASPL reflects the cumulative pressure levels across all frequency bands. Different ranges were chosen for the 2D and 3D plot in order to compare the shape of the radiation pattern. Both directivity plots show the cardioid shape, which is typical for trailing edge noise.

The increase in overall sound pressure level between  $300^\circ$  and  $330^\circ$  is owed to the virtual microphones being unable to distinguish between acoustic and vorticity modes and reflects the turbulent vortices, that can be seen in figure 5.7. The gaps in both plots occur, because in areas where the microphone circles intersect the wing profile, no microphones can be placed and therefore no data is available at these angles. These gaps also differ for the first and second microphone circle. Along the first microphone circle, 344 instead of 360 microphones were placed and  $104^\circ$  to  $120^\circ$  weren't covered by microphones. On the second circle, angles from  $110^\circ$  to  $138^\circ$  can not be evaluated, as only 332 microphones were placed on this circle. Other than the overall lower sound pressure level in the case of the 3D simulation, the sound also seems to be more strongly directed along the suction side of the flap.

The sound spectra of the trailing edge sound source were mostly evaluated for microphones on the pressure side of the flap between  $120^\circ$  and  $270^\circ$ . An evaluation between  $300^\circ$  and  $330^\circ$  would not make sense, as the acoustic fluctuations are covered by the turbulent fluctuations within the vortices moving across those microphones. A noticeable effect, visible in both directivity plots, is the signal of microphone 2 being higher than on microphone 1 at angles of  $140^\circ$  to  $150^\circ$ . An explanation for this can be found in [28]. Within that work, an examination of the trailing edge source showed that the emitted sound was reflected on the pressure side of the wing at two locations; at the corner between the main wing and the highly deflected flap, as well as at the

droop nose. Here, the computational domain does not include the droop nose, but the reflection at the corner would still occur. Microphone 2 would actually be closer to that location at  $140^\circ$  to  $150^\circ$  than microphone 1, meaning the reflected signal would have decayed less than when it reaches microphone 1.

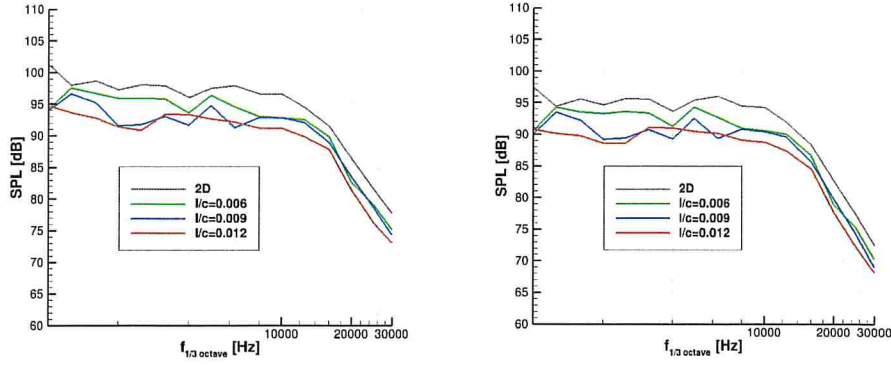


(a) Spectra of Trailing Edge Noise at  $\Theta = 0^\circ$  on Mic1 (b) Spectra of Trailing Edge Noise at  $\Theta = 0^\circ$  on Mic2

Figure 5.11: Spectra of Trailing Edge Noise at  $\Theta = 0^\circ$  on Mic1 and Mic2 for different spanwise extensions

Figure 5.11 shows the  $\frac{1}{3}$  octave sound spectra at  $\Theta = 0^\circ$  on the first and second microphone circle. The shape of the spectrum does not change, but the sound pressure levels measured on the first microphone circle are slightly higher, due to the microphone being closer to the source. The effect of spanwise expansion can also be seen. The two-dimensional simulation shows a higher amplitude of the acoustic signal across all frequencies, as the sound pressure levels of all 3D simulations stay below that of the 2D simulation. This can be explained based on the effect of the spanwise extension on the sound intensity. Equation 2.6 showed the dependence of the sound intensity of trailing edge noise on the span  $b$  of the wing. The two-dimensional simulation assumes an infinite span, resulting in higher sound pressure levels. It also assumes an infinite spanwise correlation length of the turbulent structures, meaning the effects of decorrelation and cancellation of sound sources are neglected.

One exception can be seen at a frequency of approximately 750 Hz, where the sound pressure level for the simulation with a spanwise extension of 0.009 surpasses that of the 2D simulation. This is likely due to the small recorded time frame of only 38 ms, which has a larger effect on lower frequencies, as these require more time to capture the full signal. The uncertainty thus increases for lower frequencies. This small exception can therefore likely be disregarded and ascribed to uncertainty in the recorded signals. The other simulations remain below the 2D results and the largest 3D simulation also shows a drop in the same region, though a much smaller one. The difference between the sound spectra for a spanwise extension of 0.009 and 0.012 is relatively small, with the red curve almost appearing as a smoothed-out version of the blue. This could suggest that an extension of 0.012 is very nearly sufficient to fully capture the most relevant vortices within the 3D turbulence. The difference in sound pressure levels is expected to decrease with further spanwise extension. An increase in sound pressure with further spanwise extension would indicate, that the spanwise correlation length of the turbulent vortices has been surpassed. The small decrease between the 0.009 and 0.012 spanwise extension may be a sign, that 0.012 is already close to covering the full spanwise correlation length of the relevant turbulent vortices.



(a) Spectra of Trailing Edge Noise at  $\Theta = 90^\circ$  on Mic1 (b) Spectra of Trailing Edge Noise at  $\Theta = 90^\circ$  on Mic2

Figure 5.12: Spectra of Trailing Edge Noise at  $\Theta = 90^\circ$  on Mic1 and Mic2 for different spanwise extensions

The spectra at  $\Theta = 90^\circ$  can be seen in figure 5.12. Once again, the only difference between the first and second microphone circle seems to be in a shift of the spectrum due to decaying amplitude with distance from the source. The trend towards lower sound pressure levels with a larger spanwise extension can also be seen up to an extension of 0.009. The red curve, representing an extension of 0.012, however, does not stay below the blue curve for  $l/c=0.009$ . It also appears more smooth with few shallow peaks. At higher frequencies of 8 kHz and above, however, the sound pressure levels of the largest 3D simulation present as the lowest of the four curves, while the other 3D simulations show almost equal levels. Here the blue curve appears as a smoothed-out version of the green curve. The same phenomena can be observed in almost all spectra, independent of microphone position.

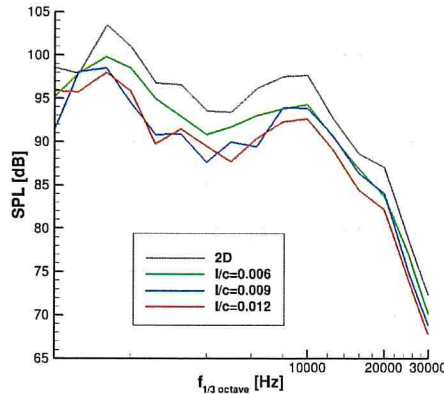
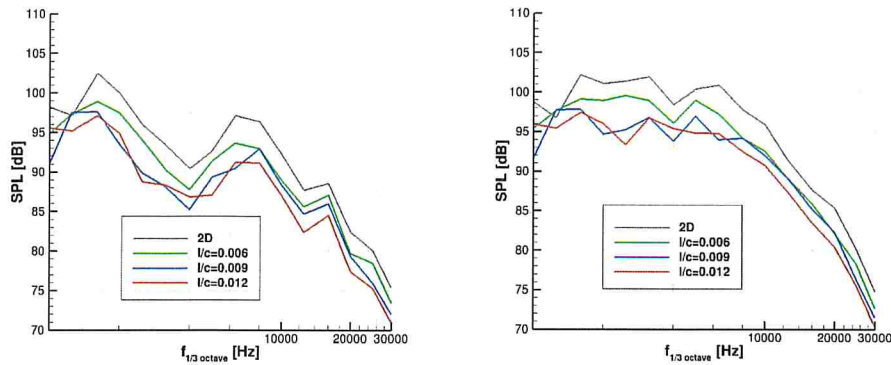


Figure 5.13: Spectra of Trailing Edge Noise at  $\Theta = 120^\circ$  on Mic1 for different spanwise extensions

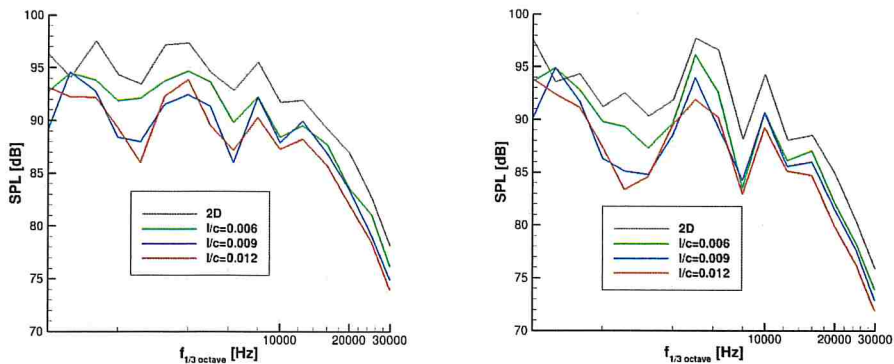
Figure 5.13 shows the sound spectra at  $\Theta = 120^\circ$  on only microphone 1, as no microphone was placed at  $120^\circ$  on the second circle due to the geometry overlap. The differences between the curves, discussed in the previous spectra, are present in this plot as well. It does, however, show a drop in sound pressure around a frequency of 4 kHz, that was not present at angles of  $0^\circ$  and  $90^\circ$ . The sound produced exclusively at the suction side of the trailing edge (as the pressure side was excluded from the source region) would need to travel around the trailing edge and upwards against the meanflow along the pressure side of the flap. The velocity gradient near



(a) Spectra of Trailing Edge Noise at  $\Theta = 140^\circ$  on Mic1 (b) Spectra of Trailing Edge Noise at  $\Theta = 140^\circ$  on Mic2

Figure 5.14: Spectra of Trailing Edge Noise at  $\Theta = 140^\circ$  on Mic1 and Mic2 for different spanwise extensions

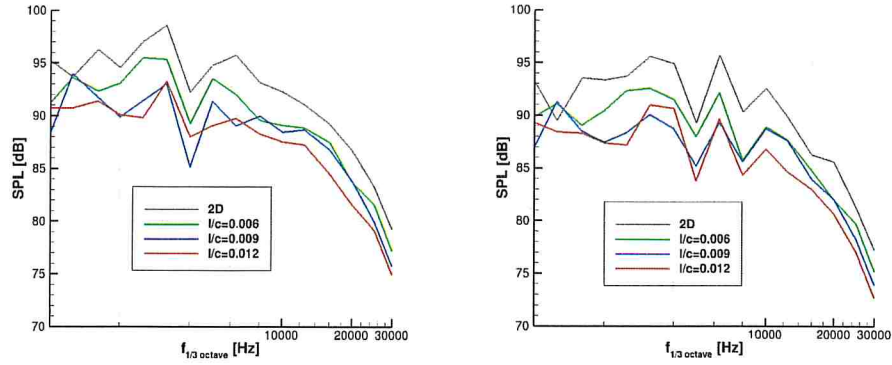
the wall, though smaller than on the suction side, may deflect sound away from the wall, where this specific microphone is placed. That dip in the spectrum is also present at  $\Theta = 140^\circ$  on microphone 1, but does not show up on microphone 2, as can be seen in figure 5.14. This would likely be the effect of the reflected sound waves filling out the deficit within the spectrum. Sound pressure levels are high in both these spectra, as the microphones are close to the maximum of the directivity plot.



(a) Spectra of Trailing Edge Noise at  $\Theta = 180^\circ$  on Mic1 (b) Spectra of Trailing Edge Noise at  $\Theta = 180^\circ$  on Mic2

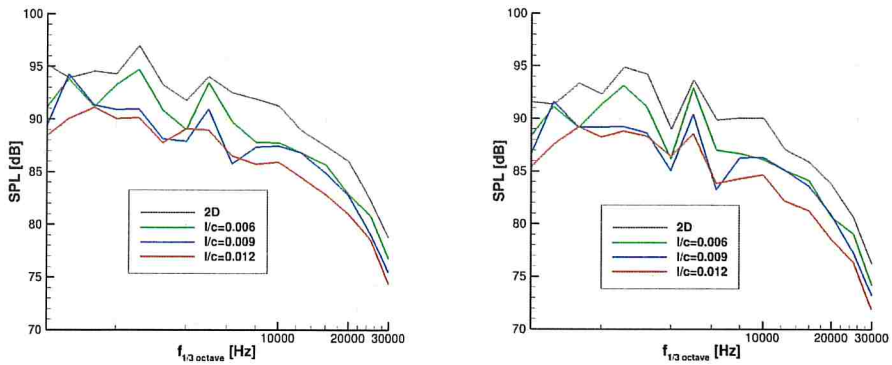
Figure 5.15: Spectra of Trailing Edge Noise at  $\Theta = 180^\circ$  on Mic1 and Mic2 for different spanwise extensions

At  $\Theta = 180^\circ$  the drop shifts towards lower frequencies and a difference can be seen between the spectra at the first and the second microphone circle. Closer to the source on Mic1, the peak of the spectra occurs at about 4 kHz. Further away, at Mic2, the peak has slightly shifted towards higher frequencies of about 5 kHz. The peaks on microphone 2 are significantly more pronounced than on microphone 1.



(a) Spectra of Trailing Edge Noise at  $\Theta = 210^\circ$  on Mic1 (b) Spectra of Trailing Edge Noise at  $\Theta = 210^\circ$  on Mic2

Figure 5.16: Spectra of Trailing Edge Noise at  $\Theta = 210^\circ$  on Mic1 and Mic2 for different spanwise extensions



(a) Spectra of Trailing Edge Noise at  $\Theta = 240^\circ$  on Mic1 (b) Spectra of Trailing Edge Noise at  $\Theta = 240^\circ$  on Mic2

Figure 5.17: Spectra of Trailing Edge Noise at  $\Theta = 240^\circ$  on Mic1 and Mic2 for different spanwise extensions

The spectra at  $\Theta = 210^\circ$  on microphone 1 (figure 5.16a) show a dip in sound pressure level at 4 kHz, which shifts towards 5 kHz in the spectra on the second microphone (figure 5.16b). The second microphone also shows another dip in the spectrum at 8 kHz, with a more pronounced peak at around 6 kHz. That peak is present at  $\Theta = 240^\circ$  as well. Here, it is also more pronounced in the spectra at microphone 2 than at microphone 1. The peak has however shifted towards 5 kHz in both spectra.

The sound radiation at  $\Theta = 270^\circ$  is particularly relevant, as it would be directed towards the ground. The spectra are shown in figure 5.18. The lower frequencies appear once again to be dominant, with sound pressure levels declining towards higher frequencies. A dip in sound pressure levels occurs at about 3 kHz. Microphones 1 and 2 show similar shapes of the spectrum with a slight reduction in sound pressure levels by the time the sound reaches the second microphone.

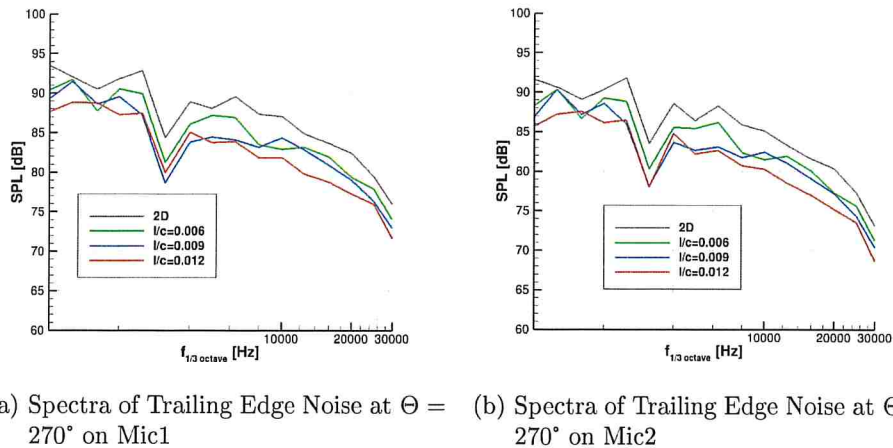


Figure 5.18: Spectra of Trailing Edge Noise at  $\Theta = 270^\circ$  on Mic1 and Mic2 for different spanwise extensions

### 5.3.2 Curvature Source

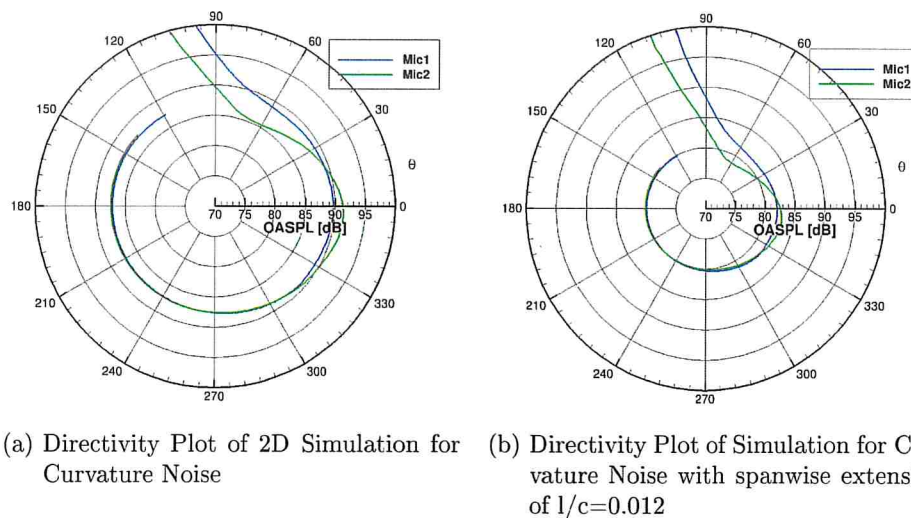


Figure 5.19: Directivity plots for Curvature Noise for 2D and largest 3D extension

The directivity plots for curvature noise once again show a decrease in overall sound pressure level compared to the 2D results. Both plots also show a significant spike in sound pressure between  $60^\circ$  and  $120^\circ$ , as the microphone circles intersect the curvature source region (see figure 5.20). The sound spectra of the corresponding microphones will thus not be compared, as the acoustic signal cannot be definitively separated from turbulent fluctuations in the source region.

The sound pressure levels on the first and second circle of microphones appear to be equal and nearly constant for angles between  $140^\circ$  and  $270^\circ$ , where noise radiation is reduced through shielding by the flap and deflected by the gradients within the various boundary layers. The fact, the signals picked up by microphones 1 and 2 are so similar is remarkable, however, and would be worth examining further. It could be connected to reflections on the pressure side once again, as well as sound being deflected due to flow gradients, away from certain microphones and towards others.



It should be marked that these plots do not accurately reflect the directivity pattern of the curvature sound source, as the microphone circles are not centered around the source but around the trailing edge. These plots are only used for determining which microphone positions are worth examining. Microphones at  $0^\circ$ ,  $30^\circ$ ,  $60^\circ$ ,  $210^\circ$ ,  $270^\circ$  and  $330^\circ$  were chosen for the spectra comparison.

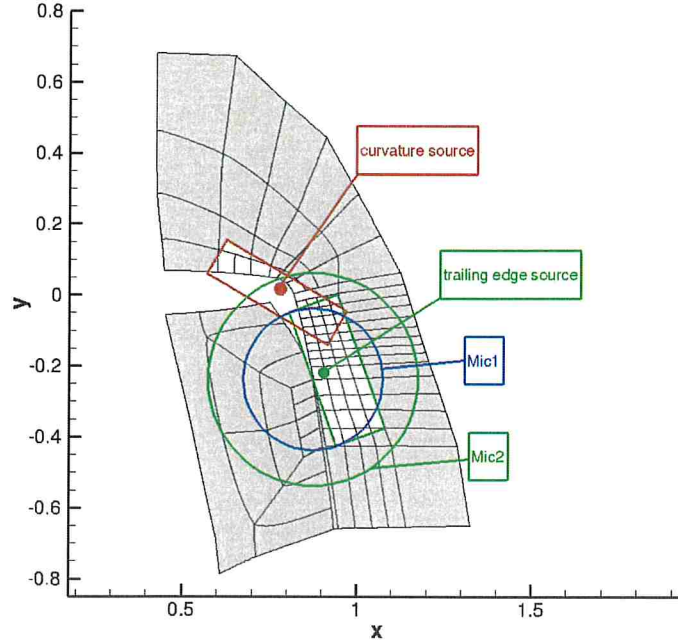
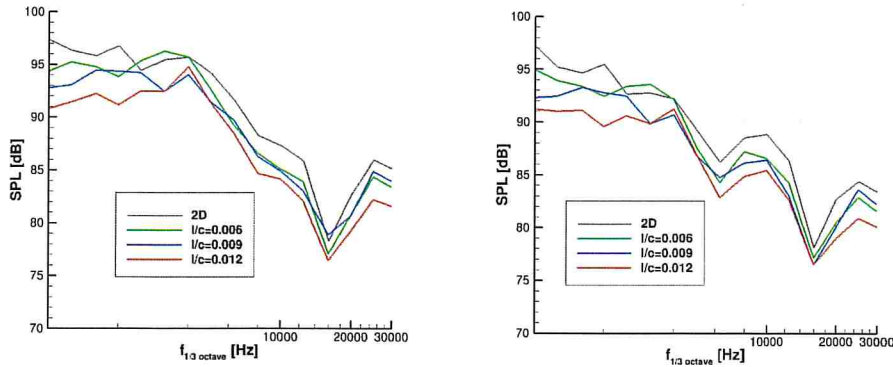


Figure 5.20: Overlap of Microphone Circles and Source Regions



(a) Spectra of Curvature Noise at  $\Theta = 0^\circ$  on Mic1 (b) Spectra of Curvature Noise at  $\Theta = 0^\circ$  on Mic2

Figure 5.21: Spectra of Curvature Noise at  $\Theta = 0^\circ$  on Mic1 and Mic2 for different spanwise extensions

Figure 5.21 shows the sound spectra at  $\Theta = 0^\circ$  from the first and second microphone circle. The decrease in sound pressure levels with spanwise extension of the simulation, which was noted in the spectra of trailing edge noise, can be seen in the curvature noise spectra as well. The shape of the spectra is similar, but the drop in sound pressure around 6 to 8 kHz is more pronounced in the second figure. The microphone further away from the trailing edge on the second circle picks up another small peak around 10 kHz. Both spectra show a drop at 16 kHz followed by a lower peak at 26 kHz. Lower frequencies up to 4 kHz are clearly dominant in both cases.

The slight differences in the shape of the spectrum between microphone 1 and microphone 2 could be related to the fact that the microphone circles are not centered around the source. Choosing two microphones at the same angle  $\Theta$ , does not necessarily reflect data in the same radiation direction at different distances, but in this case two different radiation directions. Therefore, a difference in the spectrum is to be expected. This also explains, why the sound pressure levels on microphone 2 are not much lower than on microphone 1, as was the case in the trailing edge spectra.

Another prominent feature in these two spectra, and almost all of the following, is the green spectrum of the simulation with smallest spanwise extension showing higher pressure levels than the results of the 2D simulation at frequencies between 2 and 4 kHz. This could once again be an error due to the short recorded time frame. It is presumed to be the case, as the results of the further spanwise extensions show lower sound pressure levels.

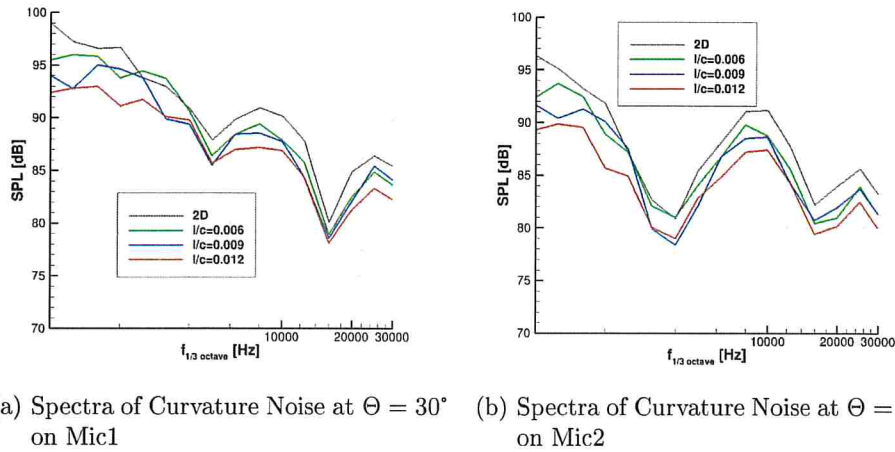


Figure 5.22: Spectra of Curvature Noise at  $\Theta = 30^\circ$  on Mic1 and Mic2 for different spanwise extensions

The Spectra at  $\Theta = 30^\circ$  are shown in figure 5.22. The shape once again varies between the two microphones. The drop at around 4 kHz, that is barely noticeable in the spectrum on Mic1, is much more pronounced at the microphone on the wider circle. Lower frequencies still dominate, but while the sound pressure levels at 1 to 4 kHz have dropped significantly by the time the second microphone is reached, the levels of the peak between 8 and 10 kHz appear to remain almost constant. Curvature noise is likely affected by deflection of sound waves that are radiated downwards along the flap surface. The gradient within the original profile boundary layer would deflect sound towards the wall, while the even stronger gradient between the jet and that boundary layer would then send sound waves away from the wall. The strongest gradient between the jet and the wall would deflect waves towards the wall, where they may be reflected, depending on the angle at which they arrive there. This complex propagation pattern of the curvature sound signals may be contributing to the varying spectra, recorded at these two microphones.

A more pronounced shift in the distribution of energy across frequencies can be seen at  $\Theta = 60^\circ$ . The spectrum at the first microphone (figure 5.23a) is dominated by frequencies below 2 kHz. The second microphone (figure 5.23b) shows a different spectrum, which is almost equally distributed across frequencies, the peak at 8 kHz being about as high or higher than the sound pressure at 1 kHz. Microphone 1 is likely picking up some turbulent fluctuations in the source region, while microphone 2 is still outside of that region, leading to higher levels on microphone 1 that do not necessarily represent the amplitude of the acoustic signal.

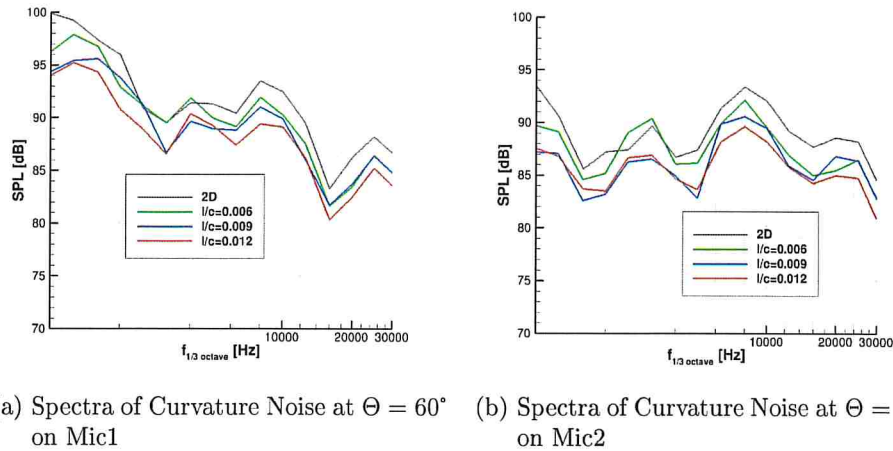


Figure 5.23: Spectra of Curvature Noise at  $\Theta = 60^\circ$  on Mic1 and Mic2 for different spanwise extensions

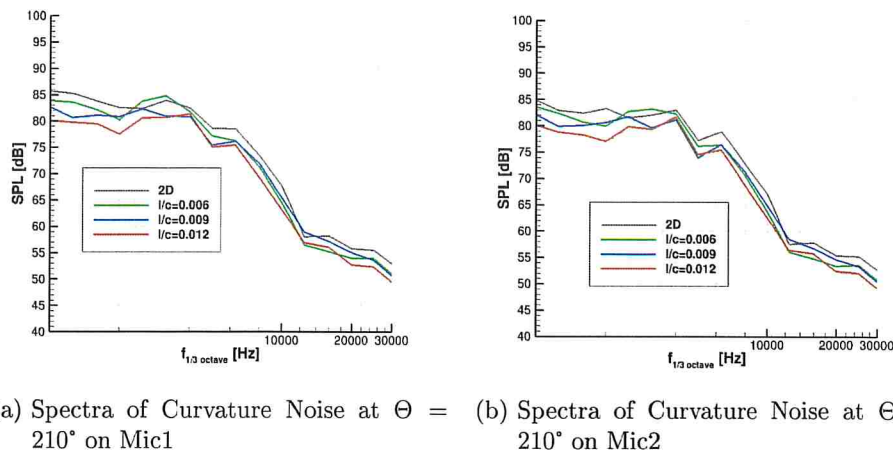
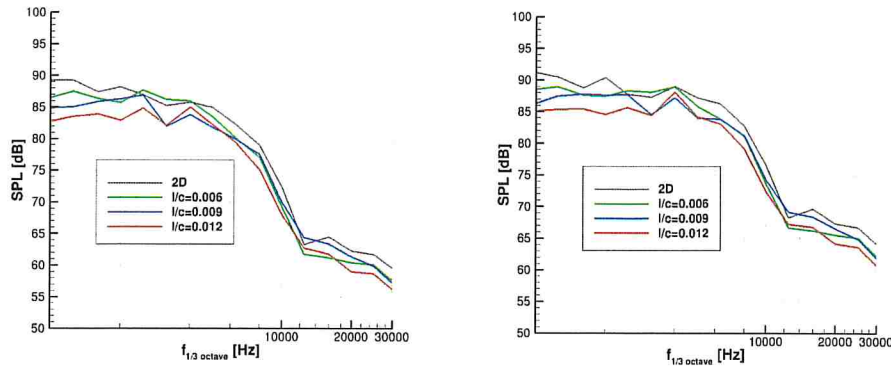


Figure 5.24: Spectra of Curvature Noise at  $\Theta = 210^\circ$  on Mic1 and Mic2 for different spanwise extensions

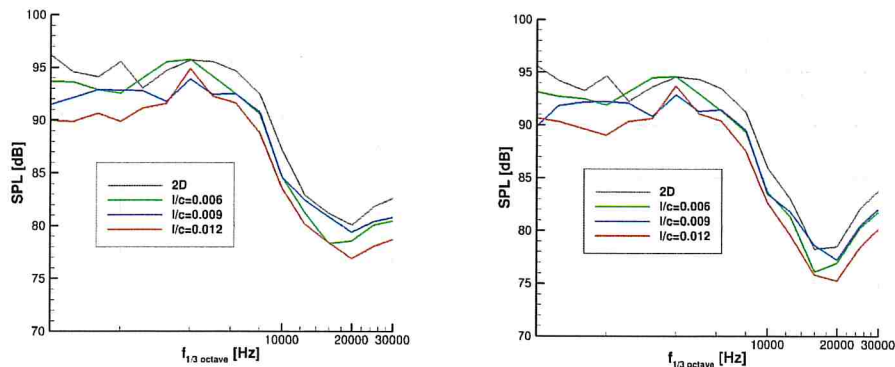
The spectra at  $\Theta = 210^\circ$  were quite different. They are shown in figure 5.24 and are meant to be representative for all angles between  $\Theta = 150^\circ$  and  $\Theta = 270^\circ$  as the spectrum does not change significantly in this region and microphones 1 and 2 do not differ much either. Lower frequencies between 1 and 4 kHz show the highest sound pressure levels with a significant decline in sound pressure at frequencies above 6 kHz. This may indicate, that the shielding effects of the flap significantly reduce the higher frequencies, while lower frequencies are able to reach the microphones as they are deflected by the velocity gradients at the trailing edge. Pressure levels at higher frequencies are slightly higher on microphone 1 than microphone 2, which is likely due to it being closer to the trailing edge. The sound waves that are able to propagate in this direction would have a smaller distance to travel, leading to less amplitude decay. It is important to remember, however, that the overall sound pressure levels are the same on microphone 1 and 2, as was seen in figures 5.19a and 5.19b.



(a) Spectra of Curvature Noise at  $\Theta = 270^\circ$  on Mic1 (b) Spectra of Curvature Noise at  $\Theta = 270^\circ$  on Mic2

Figure 5.25: Spectra of Curvature Noise at  $\Theta = 270^\circ$  on Mic1 and Mic2 for different spanwise extensions

The spectra at  $\Theta = 270^\circ$  are shown in figure 5.25, as this represents an important radiation direction for sound perceived on the ground. An interesting observation is that the sound pressure levels on microphone 2 appear to be slightly above those extracted at microphone 1, in spite of the higher distance from the source in the case of the second microphone. It may be, that sound that is deflected at the trailing edge is unable to reach the first microphone, while reflections at the pressure side experience a deflection that decreases the distance to microphone 2 but not microphone 1.



(a) Spectra of Curvature Noise at  $\Theta = 330^\circ$  on Mic1 (b) Spectra of Curvature Noise at  $\Theta = 330^\circ$  on Mic2

Figure 5.26: Spectra of Curvature Noise at  $\Theta = 330^\circ$  on Mic1 and Mic2 for different spanwise extensions

Figure 5.26 shows the sound spectra at  $\Theta = 330^\circ$ . The sound pressure levels stay between 95 and 90 dB up to frequencies of 10 kHz followed by a steep decline towards higher frequencies. The levels increase again at frequencies above 20 kHz. No shielding occurs in this direction. The spectra are thus similar in shape to the spectra at  $\Theta = 0^\circ$ , but the sound pressure levels are slightly lower as these microphones are further away from the source.

### 5.3.3 2D Correction

Section 5.3 showed, that the 2D simulations predicted higher sound pressure levels than the 3D simulation by several dB. In [37] equation 5.1 was suggested as a correction for 2D narrow band spectra. The derivation of the equation assumes the observer position to be in the far-field, which is not the case in this study. For the calculation of the correction the constant  $C = 2.1$ , the spanwise extension  $l$ , the free stream Mach number  $M = 0.15$  and the distance  $R = 0.3m$  was used for microphones on the outer circle. The distance would be  $R = 0.2m$  for microphones on the inner circle. This only applies for the trailing edge source, as the distance from the curvature source is not equal to the radius of the microphone circle, but would vary for different angles  $\Theta$ . The resulting correction for the spanwise extension of  $l/c = 0.012$  or  $l = 0.0036m$  would be  $-22$  dB for a microphone on the inner circle and  $-24$  dB on the outer circle. For smaller extensions those values would be even higher. In the case of the smallest spanwise extension of  $l/c = 0.006$  or  $l = 0.0018m$  the correction would be  $-27$  dB on the outer circle. The correction therefore does not appear to be appropriate in this case, as these correction terms are way too high. A value of around  $-5$  dB would be enough to match the 2D results to the 3D spectra, judging by the spectra examined in the previous chapter. The far-field assumption not being met in this case may be the cause for these large correction values, as the amplitude would decay differently in relation to distance in the far-field.

$$L_p(x, y, 0, \omega)|_{3D} = L_p(x, y, \omega)|_{2D} + 10 \lg \left( \frac{C l}{2\pi R} M_\infty \right) \quad (5.1)$$

As an alternative, the Oberai correction [38], which the previous correction was also derived from, was tested. As can be seen in equation 5.2 however, the original Oberai correction is frequency-dependent. This results in correction terms similar to the other correction for frequencies of 1 kHz. The correction then decreases towards 10 kHz and a small positive correction term is reached for frequencies of 20 to 30 kHz. This correction does not appear to be appropriate either, as the spectra showed a nearly uniform shift of the spectrum between 2D and 3D.

$$SPL_{3D} = SPL_{2D} + 10 \lg \left( \frac{fl}{ra_\infty} \right) \quad (5.2)$$

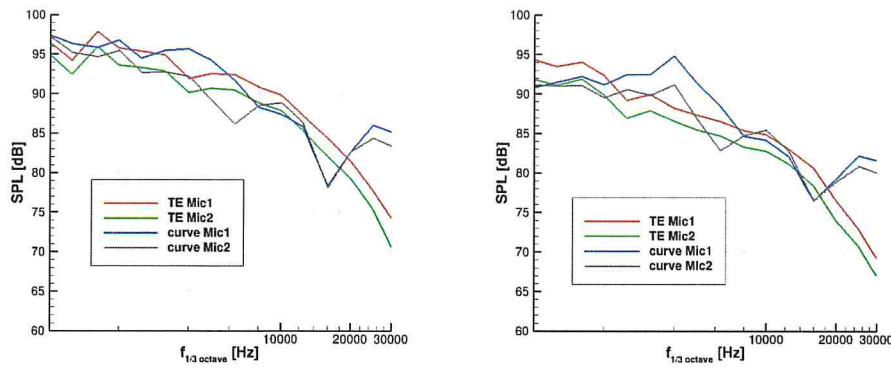
Neither of these corrections gave the desired results. It may be possible to better calibrate corrections using the 3D results presented in this thesis to arrive at more appropriate correction terms for near-field data.

### 5.3.4 Comparison of Both Sources

In this section, the spectra of trailing edge noise and curvature noise are compared and the influence of the spanwise extension of the simulation is examined.

Figure 5.27 shows the spectra in downstream direction at  $\Theta = 0^\circ$  for the 2D simulation and the largest spanwise extension of 0.012. The sound pressure levels of trailing edge noise extracted at microphone 1 are higher in both simulations than at microphone 2, reflecting the decay in amplitude with distance. This relation is more complicated in the case of curvature noise, as the microphone circles are not centered around the source region. The sound pressure levels on microphone 1 are mostly higher than microphone 2 except at frequencies of 8 to 12 kHz. This could be due to deflection of sound waves from the curvature source within the complex velocity profile near the flap surface.

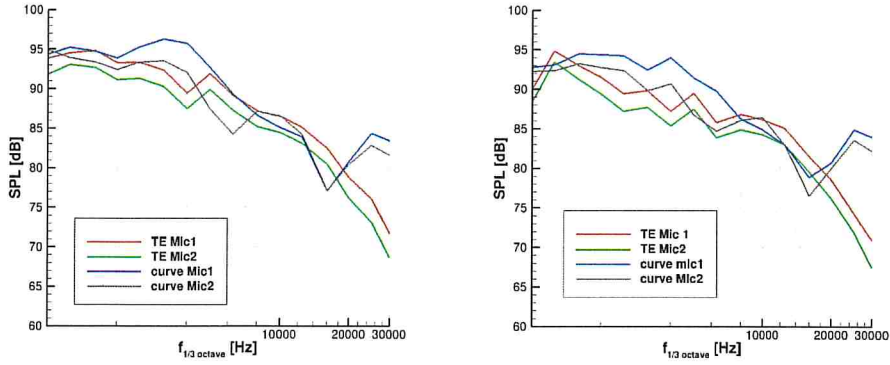
The spectra of trailing edge and curvature noise do not differ much at this radiation direction, however, curvature noise seems to be slightly higher at frequencies of around 4 kHz and frequencies above 20 kHz. Sound pressure levels are overall lower in figure 5.27b than in figure 5.27a reflecting the effects of the assumption of an infinite span and infinite correlation length on the sound pressure levels in the 2D simulation. The peak in curvature noise at 4 kHz is more pronounced in the 3D simulation results.



(a) Spectra of Trailing Edge and Curvature Noise at  $\Theta = 0^\circ$  from 2D Simulation  
 (b) Spectra of Trailing Edge and Curvature Noise at  $\Theta = 0^\circ$  from Largest 3D Simulation (0.012 spanwise extension)

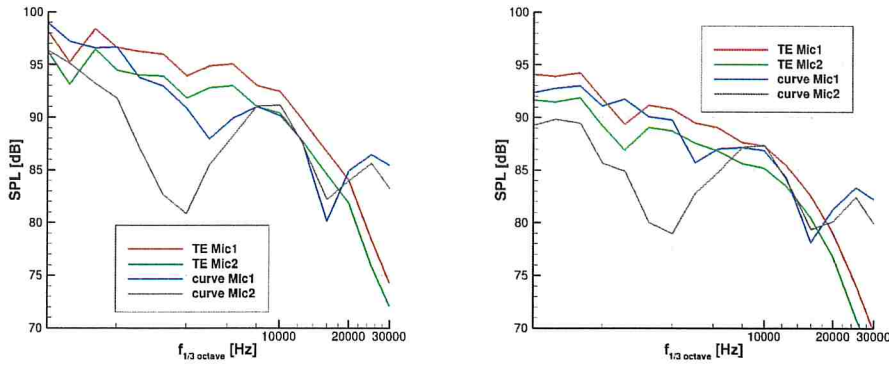
Figure 5.27: Comparison of Spectra at  $\Theta = 0^\circ$

Figure 5.28 shows the spectra at the lower spanwise expansions. The sound pressure levels decrease with larger spanwise extensions and the peak at 4 kHz does become sharper as the computational domain is extended further. The level of the peak appears to fluctuate around 95 dB. In the smallest 3D simulation the level is slightly higher than in the 2D simulation and from 0.009 to 0.012 spanwise extension, the level rises again. This could be another error due to the short time frame that was recorded, as the levels at higher frequencies show a more continuous decrease with growing spanwise extensions. Another interesting frequency range is 8 to 12 kHz, as it would appear, that with increasing spanwise expansion the sound pressure levels of curvature noise increase in relation to trailing edge noise. This may indicate, that the spanwise extension affects both sources differently.



- (a) Spectra of Trailing Edge and Curvature Noise at  $\Theta = 0^\circ$  from smallest 3D simulation (0.006 spanwise extension)
- (b) Spectra of Trailing Edge and Curvature Noise at  $\Theta = 0^\circ$  from 3D Simulation with 0.009 spanwise extension

Figure 5.28: Comparison of Spectra from smaller 3D Simulations



- (a) Spectra of Trailing Edge and Curvature Noise at  $\Theta = 30^\circ$  from 2D Simulation
- (b) Spectra of Trailing Edge and Curvature Noise at  $\Theta = 30^\circ$  from 3D Simulation with 0.012 spanwise extension

Figure 5.29: Comparison of Spectra at  $\Theta = 30^\circ$

The spectra at  $\Theta = 30^\circ$  are shown in figure 5.29. Curvature noise levels are below those of trailing edge noise with the exception of frequencies higher than 20 kHz. In the 2D simulation, curvature noise dominates at frequencies below 1 kHz but in the 3D simulation, it no longer does. In the 3D simulation, curvature noise at 2 to 3 kHz on microphone 1 slightly surpasses trailing edge noise, but at microphone 2, trailing edge noise levels are once again higher.

Figure 5.30 shows the spectra at  $\Theta = 60^\circ$ . The spanwise extension does appear to have a stronger effect on trailing edge noise, as levels do not shift equally. Instead, the spectra have moved closer together in figure 5.30b, implying that curvature noise levels were not decreased by the same amount as trailing edge noise. It should be considered, however, that at  $\Theta = 60^\circ$ , the microphones are quite close to the source region of curvature noise and microphone 1, in particular, is likely to be affected.

At  $\Theta = 90^\circ$ , both microphones are likely picking up pressure fluctuations in the curvature source region. The plots for curvature noise in figure 5.31 are therefore not an accurate representation of the upward sound radiation of this source and cannot be accurately compared to the trailing edge sound spectrum.

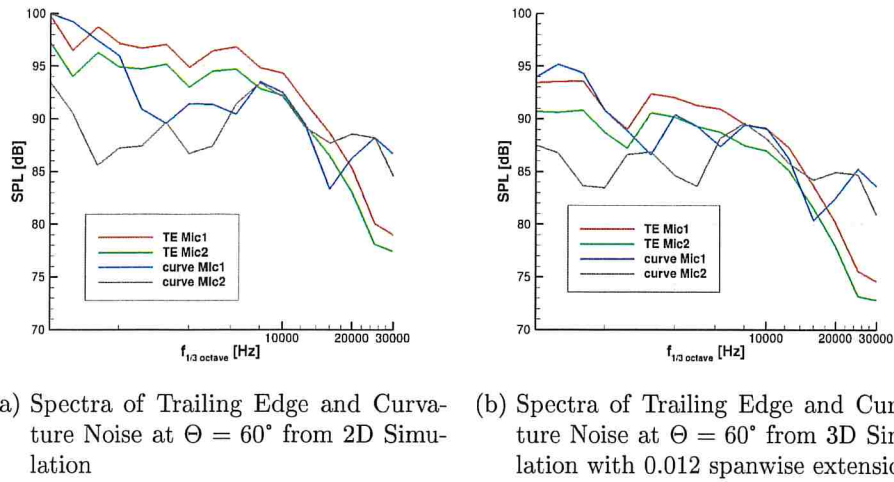
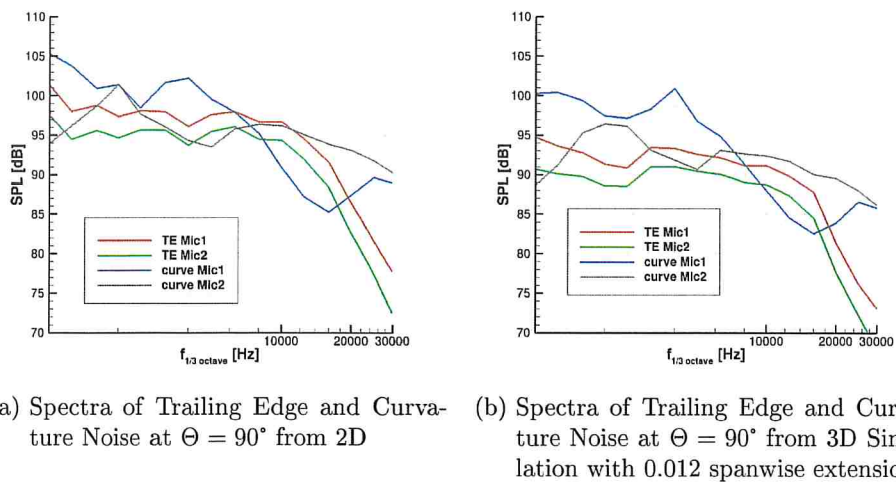
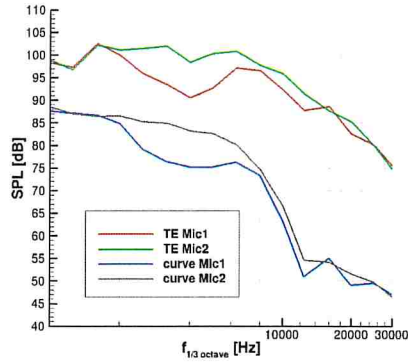
Figure 5.30: Comparison of Spectra  $\Theta = 60^\circ$ Figure 5.31: Comparison of Spectra  $\Theta = 90^\circ$ 

Figure 5.32 shows the sound spectra at  $\Theta = 140^\circ$ . At this angle, both microphones would be located below the main wing. The striking difference in sound pressure level between trailing edge and curvature noise is likely caused by shielding by the flap. The sound signal generated at the flap shoulder suffers high transmission losses before it reaches the microphone, leading to lower recorded sound pressure levels. The higher sound pressure levels on microphone 2 for both sources are likely caused by reflections at the pressure side of the wing.

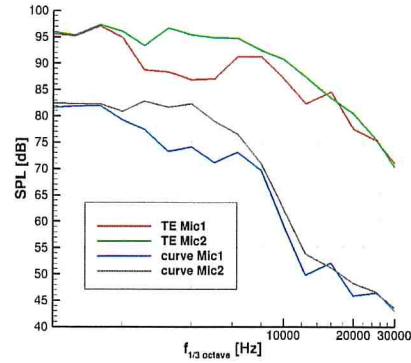
These effects are still present at  $\Theta = 180^\circ$ . Figure 5.33 shows that microphone 1 is starting to record higher levels than microphone 2, though not consistently across all frequencies. Around 5 to 6 kHz and 10 kHz, levels on microphone 2 are still slightly higher.

Figure 5.34 shows the sound spectra recorded on microphones at  $\Theta = 240^\circ$ . Microphone 1 registers higher levels of both trailing edge and curvature noise than microphone 2. Curvature noise is still lower in this region than trailing edge noise, but the gap is shrinking. It is also apparent in this figure, that the difference between curvature and trailing edge noise is lower in the 3D results. This would indicate, that curvature noise experiences less decorrelation in spanwise direction, which would decrease the sound pressure levels, than trailing edge noise.



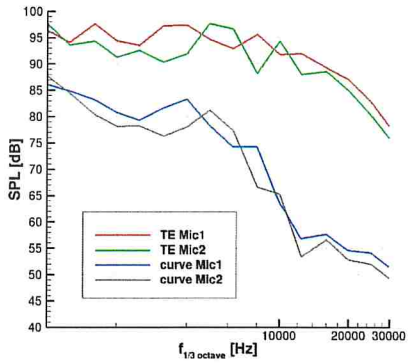


(a) Spectra of Trailing Edge and Curvature Noise at  $\Theta = 140^\circ$  from 2D

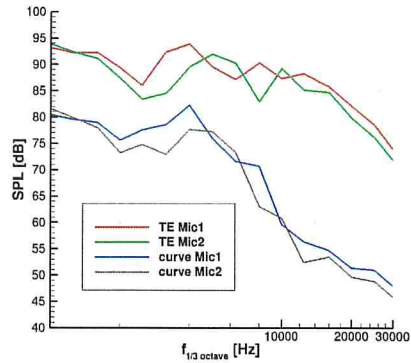


(b) Spectra of Trailing Edge and Curvature Noise at  $\Theta = 140^\circ$  from 3D Simulation with 0.012 spanwise extension

Figure 5.32: Comparison of Spectra  $\Theta = 140^\circ$



(a) Spectra of Trailing Edge and Curvature Noise at  $\Theta = 180^\circ$  from 2D

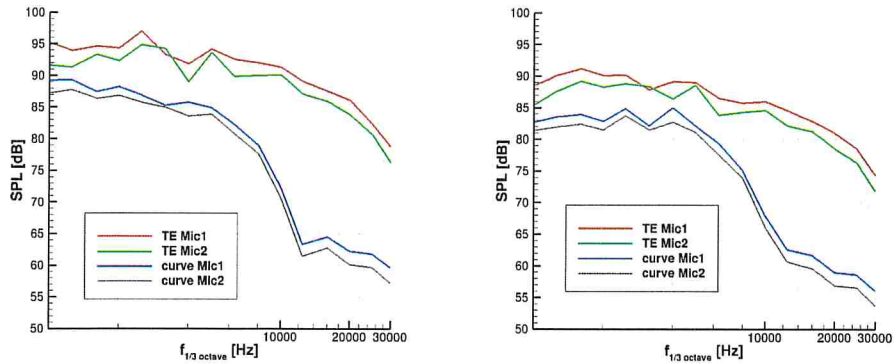


(b) Spectra of Trailing Edge and Curvature Noise at  $\Theta = 180^\circ$  from 3D Simulation with 0.012 spanwise extension

Figure 5.33: Comparison of Spectra at  $\Theta = 180^\circ$

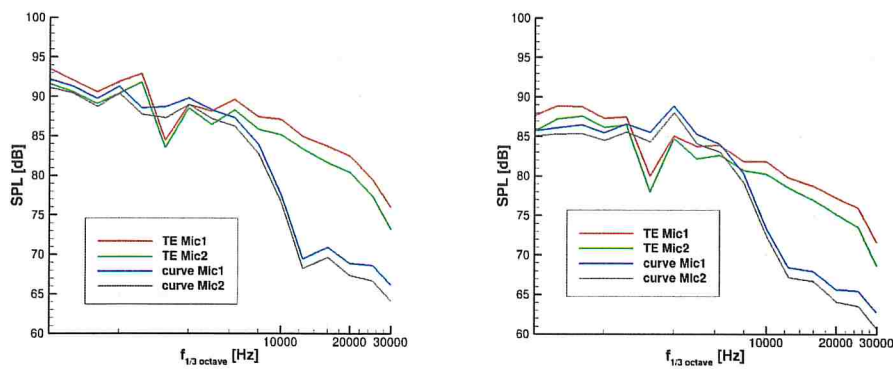
As shown in figure 5.35, at  $\Theta = 270^\circ$  trailing edge noise and curvature noise show similar levels for frequencies below 10 kHz, while at higher frequencies trailing edge noise appears to still be dominant. Curvature noise is likely affected by both shielding, as well as a higher distance between the microphones and the sound source.

$\Theta = 345^\circ$  was chosen as a downward microphone position aft of the wing, to avoid the microphones picking up turbulent fluctuations rather than acoustic signals, as would be the case between  $\Theta = 300^\circ$  and  $\Theta = 330^\circ$ . The spectra are shown in figure 5.36. The shape of the spectra is similar to  $\Theta = 0^\circ$ , though the difference in SPL between trailing edge and curvature noise is higher. Curvature noise appears to be dominant at this location in the 3D simulation results, more so than in the 2D results, for frequencies of 2 to 10 kHz and above 20 kHz. Once again, the spanwise decorrelation appears to have a stronger effect on trailing edge noise than on curvature noise.



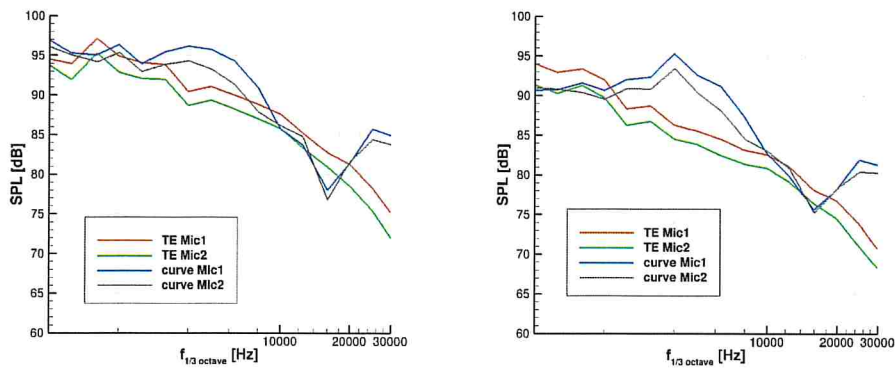
(a) Spectra of Trailing Edge and Curvature Noise at  $\Theta = 240^\circ$  from 2D (b) Spectra of Trailing Edge and Curvature Noise at  $\Theta = 240^\circ$  from 3D Simulation with 0.012 spanwise extension

Figure 5.34: Comparison of Spectra at  $\Theta = 240^\circ$



(a) Spectra of Trailing Edge and Curvature Noise at  $\Theta = 270^\circ$  from 2D (b) Spectra of Trailing Edge and Curvature Noise at  $\Theta = 270^\circ$  from 3D Simulation with 0.012 spanwise extension

Figure 5.35: Comparison of Spectra at  $\Theta = 270^\circ$



(a) Spectra of Trailing Edge and Curvature Noise at  $\Theta = 345^\circ$  from 2D (b) Spectra of Trailing Edge and Curvature Noise at  $\Theta = 345^\circ$  from 3D Simulation with 0.012 spanwise extension

Figure 5.36: Comparison of Spectra at  $\Theta = 345^\circ$

## Chapter 6

# Conclusion

In this work, curvature and trailing edge noise of a Coanda-flap were examined in three-dimensional aeroacoustic simulations with a small spanwise extension that was gradually increased. Simulations did not extend far enough to fully capture the largest turbulent vortices within the turbulent boundary layer, but the influence of the spanwise extension of the computational domain on the sound spectra was discernable from the completed simulations. Due to the small size of the computational domain, data could only be collected from virtual microphones within the near-field and sound pressure levels are not directly comparable to measurements in the acoustic far-field.

The results of this study support the findings in [13]. The 2D simulations appear to be able to capture the qualitative shape of the sound spectra with a shift in sound pressure levels of the entire spectrum, that can be adjusted for using the 2D to 3D correction term provided in [37]. Sound pressure levels are shown to decrease with the spanwise extension of the computational domain.

The effect of spanwise decorrelation on trailing edge noise appears to be slightly stronger than on curvature noise, which relates to the fact, that the smaller turbulent structures appear to be more relevant to trailing edge noise than curvature noise. More decorrelation and cancellation occurs for trailing edge noise, as more of these smaller eddies fit within the small spanwise extensions that were tested.

A dominance of trailing edge noise is seen at the lower front arc due to shielding effects on curvature noise by the flap. Lower aft noise radiation appears to be dominated by curvature noise, particularly at frequencies above 2 kHz on the full scale. This is also in agreement with [13]. These findings suggest that measures for curvature noise mitigation could be worth investigating, as a reduction in trailing edge noise would merely reduce noise radiation downwards to the front, but leave curvature and thus noise aft of the wing unaffected.

A small spanwise extension may be sufficient for capturing the most relevant parts of the three-dimensional turbulence. This may be useful, as larger spanwise extensions increase computation times significantly, but should be further verified before it can be taken as a reliable fact. Curvature noise may also require a larger spanwise extension than trailing edge noise.

If the required time is available, a few simulations with larger spanwise extension should be employed to determine the actual spanwise correlation lengths. Microphone circles around the curvature source would be useful, to get a more accurate representation of the radiation pattern and the deflection of sound within the complex velocity profile on the suction side of the flap may be useful. One might discover a way to reduce curvature noise on the ground by influencing the sound propagation, as no methods for reducing the source itself are known so far.

# Bibliography

- [1] Jan Delfs, Christina Appel, Paul Bernicke, Christopher Blech, Jason Blinstrub, Constance Heykena, Pradeep Kumar, Konstantin Kutscher, Nicolas Lippitz, Lennart Rossian, Luciana Savoni, and Markus Lummer. Aircraft and technology for low noise short take-off and landing. In *35th AIAA Applied Aerodynamics Conference*, June 2017.
- [2] David P. Lilley Lockard. The Airframe Noise Reduction Challenge. Technical report, NASA, April 2004.
- [3] International Civil Aviation Organization. ICAO Annex 16 Volume 1, 2011.
- [4] Michael Pott-Pollenske, Jochen Wild, Michaela Herr, Jan Werner Delfs, Anton Rudenko, and Alexander Büscher. Slat noise reduction by means of adaptive leading edge devices. In *Aircraft Noise Reduction by Flow Control and Active/Adaptive Techniques*, September 2014.
- [5] Michaela Herr. *Trailing-Edge Noise - Reduction Concepts and Scaling Laws*. Ph.d. thesis, Technische Universität Braunschweig, 2013. also: DLR Forschungsbericht 2013-32.
- [6] Michael Pott-Pollenske and Kai-Christoph Pfingsten. Aeroacoustic Performance of an Airfoil with Circulation Control. In *16th AIAA/CEAS Aeroacoustics Conference*, Aeroacoustics Conferences. American Institute of Aeronautics and Astronautics, June 2010.
- [7] K. C. Pfingsten, R. D. Cecora, and R. Radespiel. An experimental investigation of gapless high-lift system using circulation control. *DLRK*, 2009.
- [8] Peter K.C. Rudolph. High-Lift Systems on Commercial Subsonic Airliners. Technical report, NASA, September 1996.
- [9] Jochen Wild, Michael Pott-Pollenske, and Bjorn Nagel. An Integrated Design Approach for Low Noise Exposing High-Lift Devices. In *3rd AIAA Flow Control Conference*, Fluid Dynamics and Co-located Conferences. American Institute of Aeronautics and Astronautics, June 2006.
- [10] R. Radespiel and M. Burnazzi. Fundamentals in coanda flap design. In R. King, editor, *Active Flow and Combustion Control 2014*, pages 101–114. Springer International Publishing, 2015.
- [11] Yasim Julian Hasan. Numerical parameter study of a strake on a turboprop engine in active high-lift configuration. Technical report, DLR, February 2017.
- [12] Drew Wetzel, Fei Liu, and Louis Cattafesta. A Theoretical and Experimental Study of Broadband Circulation Control Noise. In *18th AIAA/CEAS Aeroacoustics Conference (33rd AIAA Aeroacoustics Conference)*, Aeroacoustics Conferences. American Institute of Aeronautics and Astronautics, June 2012.
- [13] Lennart Rossian, Alexandre Suryadi, Karl-Stéphane Rossignol, Roland Ewert, Michaela Herr, Jan Delfs, and Pradeep Kumar. Numerical and experimental insights into the noise

- generation of a circulation control airfoil. In *2018 AIAA/CEAS Aeroacoustics Conference*, AIAA AVIATION Forum. American Institute of Aeronautics and Astronautics, June 2018.
- [14] Michael S. Howe. Analytical Study of the Noise Generated by a Coanda Wall Jet Circulation Control Device. Technical Report AM-00-004, BOSTON UNIV MA COLL OF ENGINEERING, October 2000.
- [15] Jochen Wild. *Aerodynamik des Hochauftriebs*. Technische Universität Braunschweig, 2018.
- [16] C. P. Van Dam. The aerodynamic design of multi-element high-lift systems for transport airplanes. In *Progress in Aerospace Science*, pages 101–144, 2002.
- [17] A. M. O. Smith. High-lift aerodynamics. *Journal of Aircraft*, 12(6):501–530, 1975.
- [18] H. Coanda. Device for deflecting a stream of elastic fluid projected into an elastic fluid, September 1936. US Patent 2,052,869.
- [19] Jan Delfs. *Lecture Notes: Basics of Aeroacoustics*. Technische Universität Braunschweig, 2016.
- [20] Michael JT Smith. *Aircraft noise*, volume 3. Cambridge University Press, 2004.
- [21] Thomas F. Pope Brooks. Airfoil self-noise and prediction. Technical report, NASA, July 1989.
- [22] Lighthill MJ. On sound generated aerodynamically—i. general theory. *Proceedings of the Royal Society A*, 211, 1951.
- [23] Klaus Ehrenfried. *Strömungsakustik: Skript zur Vorlesung*. Mensch-und-Buch-Verlag, 2004.
- [24] Xavier Gloerfelt. Cavity noise. *VKI lecture series*, 3, 2009.
- [25] M.S. Howe. A review of the theory of trailing edge noise. *Journal of Sound and Vibration*, 61(3):437–465, December 1978.
- [26] Jan Delfs. Methoden der Aeroakustik. Technical report, DLR, Lecture University of Technology Braunschweig, 2007.
- [27] J. E. Ffowcs-Williams and L. H. Hall. Aerodynamic sound generation by turbulent flow in the vicinity of a scattering half plane. *Journal of Fluid Mechanics*, 40(4):657–670, 1970.
- [28] Lennart Rossian. *Minderung der Schallabstrahlung von Hochauftriebssystemen mittels aeroakustisch wirksamer poröser Materialien in Verbindung mit aktiver Strömungskontrolle*. Ph.d. thesis, Technische Universität Braunschweig, 2019.
- [29] R. Ewert and J. Delfs. Numerical Methods in Computational Aeroacoustics. *Lecture*, 2019.
- [30] R. Ewert, J. Dierke, J. Siebert, A. Neifeld, C. Appel, M. Siefert, and O. Kornow. CAA broadband noise prediction for aeroacoustic design. *Journal of Sound and Vibration*, 330(17):4139–4160, August 2011.
- [31] Roland Ewert. RPM - the fast Random Particle-Mesh method to realize unsteady turbulent sound sources and velocity fields for CAA applications. In *13th AIAA/CEAS Aeroacoustics Conference (28th AIAA Aeroacoustics Conference)*, Aeroacoustics Conferences. American Institute of Aeronautics and Astronautics, May 2007.
- [32] Jan W. Delfs, Marcus Bauer, Roland Ewert, Herwig A. Grogger, Markus Lummer, and Thomas G.W. Lauke. Numerical Simulation of Aerodynamic Noise with DLR’s aeroacoustic code PIANO, 2008.

- 
- [33] Andrej Neifeld, Christina Appel, Jürgen Dierke, Roland Ewert, and Jan W. Delfs. *CAA Prediction of Jet-Wing Interaction Noise Using Eddy Relaxation Source Model*, pages 635 – 645. Springer, 2018.
- [34] Nils Reiche, Roland Ewert, and Jan Delfs. Realization of arbitrary vorticity spectra using generic stochastic turbulence. In *22nd AIAA/CEAS Aeroacoustics Conference*, page 2964, 2016.
- [35] Joseph J Gorski and Peter S Bernard. Modeling of the turbulent enstrophy equation. *International journal of engineering science*, 34(6):699–714, 1996.
- [36] Nils Reiche, Markus Lummer, Roland Ewert, and Jan Delfs. Towards high-lift noise from fast multipole bem with anisotropic synthetic turbulence sources. In *21st AIAA/CEAS Aeroacoustics Conference*, 2015.
- [37] R. Ewert, D. Appel, J. Dierke, and M. Herr. Rans/caa based prediction of naca 0012 broadband trailing edge noise and experimental validation. *AIAA*, May 2009.
- [38] Assad A Oberai, Farzam Roknaldin, and Thomas JR Hughes. Trailing-edge noise due to turbulent flows. *AIAA Journal*, 2002.

# List of Figures

1.1	Component breakdown of noise contribution during approach for modern short to medium range transport aircraft from Airbus SILENCER project [4]	1
1.2	3-Element-Wing vs. Gapless High Lift System	2
1.3	Effect of Coanda Blowing Momentum on Generated Lift	2
2.1	Effect of leading vs trailing edge devices on the lift curve [16]	4
2.2	Coanda effect on Coanda flap [10]	5
2.3	Sound spectrum of propeller noise [20]	6
3.1	Schematic of CFD-CAA hybrid approach [13]	10
4.1	Mean Flow Field around Coanda Flap from CFD RANS	14
4.2	Starting 2D CAA mesh with trailing edge(green) and curvature(red) source region	15
4.3	Comparison of Microphone Positions on top of Previous Mesh vs. New Mesh	15
4.4	New positions of virtual microphone circles	16
5.1	Narrow band spectra for different trailing edge fRPM meshes	17
5.2	Narrow band spectra for different flap curve fRPM meshes	18
5.3	Comparison of smaller trailing edge fRPM to original fRPM	19
5.4	Comparison of smaller flap curve fRPM to original mesh with 0.001 resolution	19
5.5	Comparison of jet resolution	20
5.6	Blocks of new 2D CAA mesh with new trailing edge(green) and curvature(red) source regions	21
5.7	Reflection of turbulent vortices at radiation boundary	22
5.8	Acoustic fields from 2D simulations	22
5.9	Velocity Profile of Mean Flow Extracted at the Flap Trailing Edge	23
5.10	Directivity Plots for Trailing Edge Noise for 2D and largest 3D Extension	24
5.11	Spectra of Trailing Edge Noise at $\Theta = 0^\circ$ on Mic1 and Mic2 for different spanwise extensions	25
5.12	Spectra of Trailing Edge Noise at $\Theta = 90^\circ$ on Mic1 and Mic2 for different spanwise extensions	26
5.13	Spectra of Trailing Edge Noise at $\Theta = 120^\circ$ on Mic1 for different spanwise extensions	26
5.14	Spectra of Trailing Edge Noise at $\Theta = 140^\circ$ on Mic1 and Mic2 for different spanwise extensions	27
5.15	Spectra of Trailing Edge Noise at $\Theta = 180^\circ$ on Mic1 and Mic2 for different spanwise extensions	27
5.16	Spectra of Trailing Edge Noise at $\Theta = 210^\circ$ on Mic1 and Mic2 for different spanwise extensions	28
5.17	Spectra of Trailing Edge Noise at $\Theta = 240^\circ$ on Mic1 and Mic2 for different spanwise extensions	28
5.18	Spectra of Trailing Edge Noise at $\Theta = 270^\circ$ on Mic1 and Mic2 for different spanwise extensions	29
5.19	Directivity plots for Curvature Noise for 2D and largest 3D extension	29
5.20	Overlap of Microphone Circles and Source Regions	30
5.21	Spectra of Curvature Noise at $\Theta = 0^\circ$ on Mic1 and Mic2 for different spanwise extensions	30
5.22	Spectra of Curvature Noise at $\Theta = 30^\circ$ on Mic1 and Mic2 for different spanwise extensions	31

---

5.23	Spectra of Curvature Noise at $\Theta = 60^\circ$ on Mic1 and Mic2 for different spanwise extensions . . . . .	32
5.24	Spectra of Curvature Noise at $\Theta = 210^\circ$ on Mic1 and Mic2 for different spanwise extensions . . . . .	32
5.25	Spectra of Curvature Noise at $\Theta = 270^\circ$ on Mic1 and Mic2 for different spanwise extensions . . . . .	33
5.26	Spectra of Curvature Noise at $\Theta = 330^\circ$ on Mic1 and Mic2 for different spanwise extensions . . . . .	33
5.27	Comparison of Spectra at $\Theta = 0^\circ$ . . . . .	35
5.28	Comparison of Spectra from smaller 3D Simulations . . . . .	36
5.29	Comparison of Spectra at $\Theta = 30^\circ$ . . . . .	36
5.30	Comparison of Spectra $\Theta = 60^\circ$ . . . . .	37
5.31	Comparison of Spectra $\Theta = 90^\circ$ . . . . .	37
5.32	Comparison of Spectra $\Theta = 140^\circ$ . . . . .	38
5.33	Comparison of Spectra at $\Theta = 180^\circ$ . . . . .	38
5.34	Comparison of Spectra at $\Theta = 240^\circ$ . . . . .	39
5.35	Comparison of Spectra at $\Theta = 270^\circ$ . . . . .	39
5.36	Comparison of Spectra at $\Theta = 345^\circ$ . . . . .	39



# List of Tables

Appendix A

Appendix